



JGR Solid Earth

RESEARCH ARTICLE

10.1029/2023JB026558

Key Points:

- Changes in hydraulic diffusivity and pressurization factor during thermal pressurization (TP) balance each other in low permeability and low porosity fault rocks
- Hydraulic diffusional length scales as time^{0.7} when considering TP parameters that depend on temperature and pressure
- The constant case model should be considered with ambient initial conditions and not time-averaged ones

Supporting Information:

Supporting Information may be found in the online version of this article.

Correspondence to:

N. Z. Badt, nbadt@sas.upenn.edu

Citation:

Badt, N. Z., Huber, C., Hirth, G., & Tullis, T. E. (2023). The pressure- and temperature-dependence of thermal pressurization in localized faults. *Journal of Geophysical Research: Solid Earth*, 128, e2023JB026558. https://doi.org/10.1029/2023JB026558

Received 14 FEB 2023 Accepted 2 AUG 2023

Author Contributions:

Conceptualization: Nir Z. Badt, Christian Huber, Greg Hirth Formal analysis: Nir Z. Badt Methodology: Nir Z. Badt, Christian Huber, Greg Hirth, Terry E. Tullis Supervision: Christian Huber, Greg Hirth, Terry E. Tullis Visualization: Nir Z. Badt Writing – original draft: Nir Z. Badt Writing – review & editing: Nir Z. Badt, Christian Huber, Greg Hirth, Terry E.

© 2023. American Geophysical Union. All Rights Reserved.

The Pressure- and Temperature-Dependence of Thermal Pressurization in Localized Faults

Nir Z. Badt¹, Christian Huber¹, Greg Hirth¹, and Terry E. Tullis¹

¹Brown University, Providence, RI, USA

Abstract Thermal pressurization (TP) is predicted to be an important dynamic frictional weakening mechanism during earthquakes. The prevailing models, though, assume that the physical, thermal and hydraulic properties of the fluid-saturated rock in the fault zone are constant during TP (the *constant case*) which inherently involves temperature and pressure changes. We solve the governing equations for TP in their general form with pressure- and temperature-dependent physical, thermal and hydraulic parameters of a saturated fault zone with a one-dimensional numerical model (the *variable case*). The model considers slip on a plane at a constant rate, and so does not account for dynamic frictional rupture scenario. We test a wide range of medium permeabilities of 10^{-22} – 10^{-16} m² and porosities 0.5%–17%, based on experimental data for Frederick diabase, Westerly granite and the Hanaore Fault gouge. We find that the predicted shear stress drop and temperature rise is similar between the two cases for low permeability (< 10^{-20} m²) and low porosity (<1%) fault rocks, owing to an increase in the fluid pressurization factor and hydraulic diffusivity. Differences between the two models are evident in more permeable and porous fault rocks. The increase in hydraulic diffusivity during TP results in a diffusional length which scales with time^{0.7} in the variable case. In addition, our calculations show that it is important to apply the constant case model with the ambient initial conditions for the modeled fault zone and not time-averaged values that aim to represent the temperature and pressure changes that occur during TP.

Plain Language Summary Thermal pressurization (TP) is a dynamic frictional weakening mechanism that is predicted to operate during earthquakes. TP activates when frictional heat causes the fluids in the pores of the rocks to pressurize due to differences in thermal expansivity between fluids and rocks. The elevated pore pressure decreases the frictional resistance during sliding. The current models for TP assume that the properties of the fault rocks and fluids are constant (the *constant case*), whereas in practice, these properties vary due to temperature and pressure changes during TP. We solve the general form of the governing equations for TP with a one-dimensional numerical model with pressure- and temperature-dependent fluid and rock properties (the *variable case*). We compare the two models for different fault rocks that span a wide range of hydraulic properties. Our results show that for low permeability (<10⁻²⁰ m²) and low porosity (<1%) rocks the two cases are similar. However, for more permeable and porous rocks the two models differ with continuous fault slip. Furthermore, we find that it is important to apply ambient initial conditions in the constant case model, rather than some time-averaged conditions that aim to compensate for the lack of sensitivity to pressure and temperature changes.

1. Introduction

Faults within fluid-saturated rocks are likely to experience frictional weakening by a process called *thermal pressurization* (TP) (Kanamori et al., 2000; Lachenbruch, 1980; Lee & Delaney, 1987; Mase & Smith, 1987; Rice, 2006; Sibson, 1973), hereafter abbreviated as *TP*. Frictional weakening during seismic slip (e.g., Tullis, 2015) can limit the temperature rise from shear heating, and thus prevent frictional melting of the country rocks. Field observations of many exhumed seismogenic fault zones show little evidence of melt in the form of pseudotachylyte (Sibson, 1973) which suggests that frictional weakening mechanisms play an important role during earthquakes. Furthermore, research into the formation of pseudotachylytes suggests that these rock formations are typically associated with dry, low-porosity crystalline rocks (Sibson, 1975; Sibson et al., 2006). The occurrence of pseudotachylytes in fault zones is still subject to further research as some studies suggest that frictional-melts may be more common than previously thought. Field studies indicate that pseudotachylytes are rarely preserved in fault zones due to chemical alterations over time or are simply underreported because of their fine texture and small scale (Fondriest et al., 2020; Kirkpatrick et al., 2009; Kirkpatrick & Rowe, 2013; Phillips et al., 2019). Other studies suggest that TP may control earthquake rupture propagation into zones where stable

BADT ET AL. 1 of 22

frictional sliding is expected to dominate (Faulkner et al., 2011; Fujiwara et al., 2011), which has a direct effect on the size and magnitude of an earthquake and the occurrence of tsunamis, when the rupture breaks to the ocean floor. TP has been suggested as an important frictional weakening mechanism during earthquakes (e.g., Rice, 2006) that can be activated even at sub-seismic slip rates of millimeters-per-second (Badt et al., 2020). The results of models of TP also provide an explanation for the observed fracture energy of real seismic events over seven orders-of-magnitude of fault slip (Viesca & Garagash, 2015).

TP is the process of pressurizing the intergranular and crack-filling pore fluids during heating—leveraging the mechanical-work-associated thermal expansion (Lachenbruch, 1980). Frictional heat produced by a slipping fault raises the temperature of the surrounding porous, fluid-saturated country rock. If the fluid is effectively trapped in the fault zone due to low permeability of the rocks, its expansion will increase pore pressure as the thermal expansion of the fluid far-exceeds that of rocks (Lachenbruch, 1980; Mase and Smith, 1984, 1987; Rice, 2006; Sibson, 1973). The increase in pore fluid pressure (p) decreases the shear stress (τ) in the matrix by counteracting the normal stress (σ) :

$$\tau = \mu(\sigma - p),\tag{1}$$

where μ is the coefficient of friction. For TP to be effective during fault slip the characteristic time for TP must be smaller than the slip duration of the fault (Mase & Smith, 1987). The characteristic time for TP depends on the slip rate, coefficient of friction, and the thermal and hydraulic characteristics of the medium (Mase & Smith, 1987). Lachenbruch (1980) derived and analyzed the governing equations for TP for special cases and calculated that for fault rocks of permeability $<10^{-13}$ m² TP will be efficient enough to promote frictional weakening. Mase and Smith (1987) predicted that TP is effective for faults with permeability $<10^{-14}$ m² or with a compressibility $<10^{-8}$ Pa⁻¹, or when shear strain is more than one. While Mase and Smith (1987) considered localized faults over a wide range of poroelastic and hydraulic properties their model considers constant hydraulic properties (e.g., permeability) and does not include the effects of specific pressure- and temperature-dependent paths of hydraulic properties.

Fault zones are heterogenous and complex geological structures, often made up of multiple slip surfaces, secondary fault planes and fractures hosted within lithologies of different mechanical properties (e.g., Faulkner et al., 2010). In addition to intrinsic heterogeneities, the physical, thermal and hydraulic properties of the rocks and pore fluids (usually water) in the fault zones respond dynamically to temperature and pressure changes during slip. Temperature and effective pressure inherently change during TP, though most of the calculations and predictions of frictional weakening during seismic slip based on the TP model assume constant thermal and hydraulic properties (e.g., Andrews, 2002; Bizzarri & Cocco, 2006; Brantut & Mitchell, 2018; Lachenbruch, 1980; Rice, 2006). In addition, some studies that investigate aspects of the temperature and pressure effect on the physical properties of fault zones, do not specifically address the underlying thermal-hydraulic-mechanical feedbacks in the TP model (Noda & Shimamoto, 2005; Wibberley & Shimamoto, 2005). Acosta et al. (2018) tested the effects of fluid thermodynamics with temperature and pressure on TP and showed that when pore water remains in liquid state TP is activated during stick-slip motion. Noda and Lapusta (2010) explored the effects of spatially heterogeneous hydraulic diffusivity on earthquake rupture simulations with TP, showing a complex earthquake sequence and spatial variability of coseismic slip. Stathas and Stefanou (2023) studied the effects of shear localization and hydraulic structure on a simulated fault weakening by TP, showing that shear localization can migrate within the deforming layer during TP. While these studies accounted for complexities of natural fault zones within the TP framework, they still impose constant hydraulic and thermal diffusivities and do not incorporate the effects of specific pressure- and temperature-dependent paths of hydraulic properties (e.g., permeability). Our work expands on the studies mentioned above to consider more realistic physical conditions for TP.

We explore how the temperature- and pore pressure-dependence of the fault zone rock and pore fluid properties affect frictional weakening and the temperature rise during fault slip. The model focuses on the dynamic behavior of a slipping fault patch after the rupture front has passed (Brantut, 2021; Garagash, 2012). Our analysis considers the pressure- and temperature-dependent paths of thermal and hydraulic properties, such as permeability. Here, we study the effects of highly variable properties during TP, which can vary over several orders of magnitude even with modest variations in effective stress and temperature (e.g., Badt et al., 2020; Noda & Shimamoto, 2005). We model TP in a fault made up of a principal slip surface (Figure 1), where deformation and heat production are localized, surrounded by a homogenous, porous material (crystalline rock or fault gouge)—as observed in field studies of localized, seismogenic faults (e.g., F. M. Chester & Chester, 1998; Faulkner et al., 2010; Sibson, 2003; Wibberley & Shimamoto, 2003). The fault model approximates the principal slip surface as a mathematical plane with zero thickness, following Mase

BADT ET AL. 2 of 22

21699356, 2023, 8, Downloaded from https://agupubs.onlinelibrary.wiley.com/doi/10.1029/2023JB026558 by Brown University Library, Wiley Online Library on [31/08/2023]. See

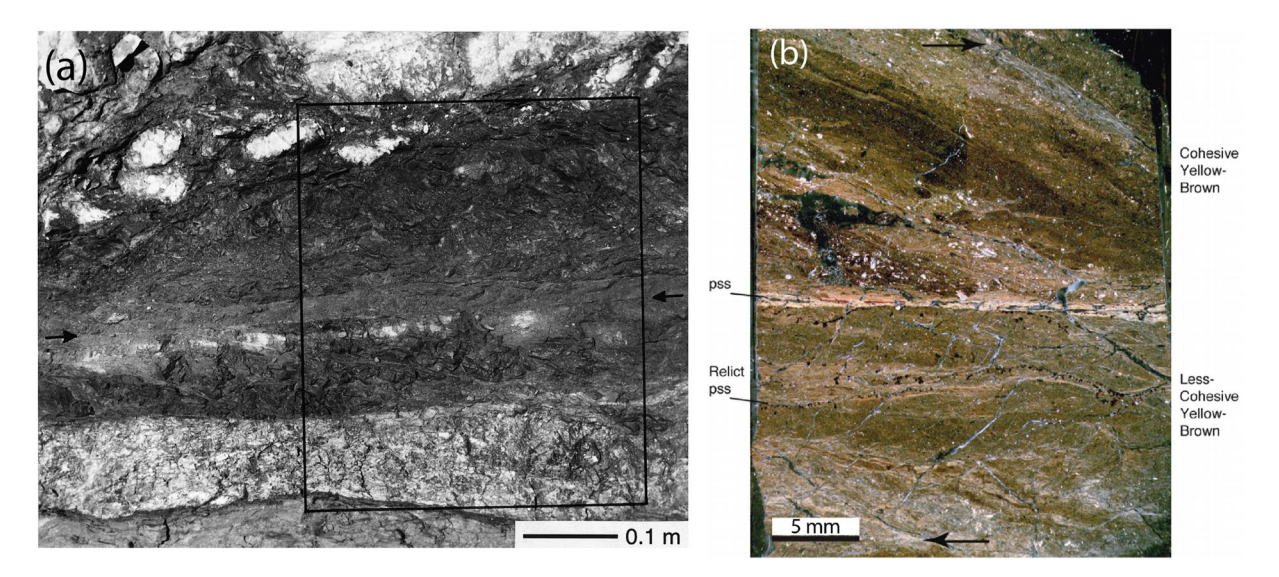


Figure 1. Punchbowl fault in California: (a) photograph of the ultracataclasite layer (darker color) located between the country rock (crystalline on top and sandstone on bottom), arrows point to the principal slip surface (pss) at the center of the ultracataclasite layer (F. M. Chester & Chester, 1998); (b) photomicrograph of the pss and the adjacent cataclasite (J. S. Chester & Goldsby, 2003).

and Smith (1984) and Rice (2006), whereas in practice the slip surface has some finite thickness which depends on the grain size of the deforming material (Rice, 2006). Furthermore, we make the simplification that the thermal and hydraulic properties across the model domain are uniform (Aydin, 2000; Passelègue et al., 2014). We compare our analysis to the classical TP model proposed by Rice (2006) and specifically the elegant analytical solution to the slip-on-plane scenario for TP, calculated assuming constant hydraulic and thermal properties.

2. Model

The TP model is based on the conservation of energy (Equation 2) and fluid-mass (Equation 3) in a porous medium. The basic assumptions are that pore fluid diffuses through a permeable medium according to Darcy's law while neglecting heat transport by fluid transport (Mase & Smith, 1987; Rice, 2006), as shown in the energy equation. The governing equations for fluid-mass and thermal energy conservation for TP were derived by Rice (2006). We assume slip is localized on a plane (hereafter referred to as the fault plane) with zero thickness; fault slip velocity, normal stress and coefficient of friction are all held constant, to comply with the assumptions made by Rice (2006).

The governing equations for the evolution of temperature (T) and pore pressure (p) in a porous medium (rock + fluid) are:

$$\frac{\partial T}{\partial t} = \frac{1}{\rho c} \left[\tau \dot{\gamma} + \frac{\partial}{\partial x} \left(K \frac{\partial T}{\partial x} \right) \right],\tag{2}$$

$$\frac{\partial p}{\partial t} = \Lambda \frac{\partial T}{\partial t} + \frac{1}{S\rho_f} \frac{\partial}{\partial x} \left(\frac{k\rho_f}{\eta} \frac{\partial p}{\partial x} \right), \tag{3}$$

where t is time, ρ is the density of the medium, c is the heat capacity of the medium, γ is the shear strain rate ($\dot{\gamma} = v/w$, where v is the fault slip velocity and w is the width of the deforming zone within the fault zone fault), K is the thermal conductivity of the medium, Λ is the pressurization factor, ρ_f is the density of the pore fluid, S is the storage capacity of the medium, k is the permeability of the medium and η is the dynamic viscosity of the pore fluid. The pressurization factor (Rice, 2006) is defined as

$$\Lambda = \frac{\alpha_f - \alpha_\phi}{\beta_f + \beta_\phi},\tag{4}$$

where α is the thermal expansion coefficient and β is the compressibility, subscripts f and ϕ denote the fluid (water) and pore space, respectively. Note that Λ is equivalent to Γ in Mase and Smith's (1987) derivation. We explore two cases: (a) constant thermal and hydraulic properties during TP—the *constant case*; and (b)

BADT ET AL. 3 of 22

variable thermal and hydraulic properties during TP—the *variable case*. The *constant case* is used to compare our model to Rice's (2006) analytical solution for TP for slip-on-a-plane. The *variable case* expands Rice's (2006) derivation to account for more realistic thermal and hydraulic conditions in the fault zone, where hydraulic properties (i.e., permeability, porosity) are strong functions of the effective stress ($\sigma - p$) and thermoelastic properties (i.e., fluid compressibility) are strong functions of temperature. The *variable case* does not admit an analytical solution and requires numerical approximation. We implement an iterative, explicit flux-conservative, numerical scheme, where all simulations start with a homogenous ambient temperature T_0 and pore pressure p_0 distribution. The codes for these simulations are available online at Badt (2023).

2.1. Constant Hydraulic Properties (Constant Case)

The model is first compared to Rice's (2006) analytical solution for slip on a plane (fault with zero thickness); this is done to calibrate the numerical model and estimate numerical errors. To do this, all the physical properties of the fluid and porous medium in Equations 2 and 3 are held constant, thus simplifying these equations to their diffusion-like form:

$$\frac{\partial T}{\partial t} = \frac{\tau \dot{\gamma}}{\rho c} + \kappa \frac{\partial^2 T}{\partial x^2},\tag{5}$$

$$\frac{\partial p}{\partial t} = \Lambda \frac{\partial T}{\partial t} + \omega \frac{\partial^2 p}{\partial x^2},\tag{6}$$

where $\kappa = K/\rho c$ and $\omega = k/S\eta$ are the thermal and hydraulic diffusivities, respectively. These equations are solved iteratively by a forward (in time) finite-difference scheme with an adaptive time step. In each iteration, the output from Equation 5 is substituted in Equation 6 until the temperature and pressure fields converge locally to within a set tolerance (here relative tolerance is set to 10^{-9}).

Rice (2006) finds an analytical solution for Equations 5 and 6 on the fault plane (x = 0), and provides expressions for the evolution of the temperature and pore fluid pressure as a function of slip (δ):

$$T = T_0 + \left(1 + \sqrt{\frac{\omega}{\kappa}}\right) \frac{(\sigma - p_0)}{\Lambda} \left[1 - \exp\left(\frac{\delta}{L^*}\right) \operatorname{erfc}\left(\sqrt{\frac{\delta}{L^*}}\right)\right],\tag{7}$$

$$p = p_0 + (\sigma - p_0) \left[1 - \exp\left(\frac{\delta}{L^*}\right) \operatorname{erfc}\left(\sqrt{\frac{\delta}{L^*}}\right) \right], \tag{8}$$

where L^* is a characteristic length scale for TP defined by Rice (2006) as:

$$L^* = \frac{4}{\mu^2} \left(\frac{\rho c}{\Lambda}\right)^2 \frac{\left(\sqrt{\omega} + \sqrt{\kappa}\right)^2}{v} \,. \tag{9}$$

The evolution of shear stress at the fault plane is then calculated by substituting Equation 8 in Equation 1:

$$\tau = \mu(\sigma - p_0) \exp\left(\frac{\delta}{L^*}\right) \operatorname{erfc}\left(\sqrt{\frac{\delta}{L^*}}\right). \tag{10}$$

For the *constant case*, numerical errors (for temperature and pore pressure) are calculated by comparing the numerical model outputs with constant hydraulic parameters to the analytical solution given in Equations 7–9.

2.2. Variable Hydraulic and Thermal Properties (Variable Case)

The effects of variable hydraulic and thermal properties are studied by solving the governing equations for TP in their most general form (Equations 2 and 3). Like the constant parameters case, these equations are solved numerically with an iterative, flux-conservative, finite-difference method. The variable hydraulic and thermal properties and their respective equations used in the model are summarized in Table 1. Three key differences distinguish the *variable case* from the *constant case*: (a) transport-related properties (K, k, η , and S) and the pressurization factor Λ are functions of pore pressure and/or temperature (Table 1); (b) the thermal conductivity remains within the spatial derivative in Equation 2 and is a function of pore pressure; and (c) the permeability, dynamic viscosity,

BADT ET AL. 4 of 22

| 803×10^{-23} Bg 803×10^{-23} Bg 83×10^{-20} Bg 83×10^{-20} Nass 9021×10^{-20} Nass 9099 CG 9099 CG 9099 CG 9099 Signary Rer Rer 9099 Signary | Physical, Hydraulic and Thermal Properties and Relations in the Model | the Model | |
|--|---|---|--|
| $k = 4.493 \times 10^{-3} (\sigma - p)^{-1.38} + 9.803 \times 10^{-2}$ $k = 2.88 \times 10^{-3} (\sigma - p)^{-1.38} + 2.58 \times 10^{-2}$ $k = 1.396 \times 10^{-3} (\sigma - p)^{-1.38} + 2.28 \times 10^{-2}$ $k = 1.396 \times 10^{-3} (\sigma - p)^{-1.38} + 0.021 \times 10^{-2}$ $k = 1.396 \times 10^{-3} (\sigma - p)^{-1.38} + 0.021 \times 10^{-2}$ $k = -9.702 \times 10^{-3} (\sigma - p)^{-1.38} + 0.021 \times 10^{-2}$ $k = -9.702 \times 10^{-3} (\sigma - p)^{-1.38} + 0.021 \times 10^{-3}$ $k = -9.702 \times 10^{-3} (\sigma - p)^{-1.38} + 0.021 \times 10^{-3}$ $k = -9.702 \times 10^{-3} (\sigma - p)^{-1.38} + 0.021 \times 10^{-3}$ $k = -9.702 \times 10^{-3} (\sigma - p)^{-1.38} + 0.021 \times 10^{-3}$ $k = -0.1719 (\sigma - p)^{-1.38} + 0.021 \times 10^{-3}$ $k = -0.1719 (\sigma - p)^{-1.38} + 0.021 \times 10^{-3}$ $k = -0.1719 (\sigma - p)^{-1.38} + 0.021 \times 10^{-3}$ $k = -0.1719 (\sigma - p)^{-1.38} + 0.021 \times 10^{-3}$ $k = -0.1719 (\sigma - p)^{-1.38} + 0.021 \times 10^{-3}$ $k = -0.1719 (\sigma - p)^{-1.38} + 0.021 \times 10^{-3}$ $k = -0.1719 (\sigma - p)^{-1.38} + 0.021 \times 10^{-3}$ $k = -0.1719 (\sigma - p)^{-1.38} + 0.021 \times 10^{-3}$ $k = -0.1719 (\sigma - p)^{-1.38} + 0.021 \times 10^{-3}$ $k = -0.1719 (\sigma - p)^{-1.38} + 0.021 \times 10^{-3}$ $k = -0.1719 (\sigma - p)^{-1.38} + 0.021 \times 10^{-3}$ $k = -0.1719 (\sigma - p)^{-1.38} + 0.021 \times 10^{-3}$ $k = -0.1719 (\sigma - p)^{-1.38} + 0.021 \times 10^{-3}$ $k = -0.1719 (\sigma - p)^{-1.38} + 0.0219 \times 10^{-3}$ $k = -0.1719 (\sigma - p)^{-1.38} + 0.0219 \times 10^{-3}$ $k = -0.1719 (\sigma - p)^{-1.38} + 0.0219 \times 10^{-3}$ $k = -0.01719 (\sigma - p)^{-1.38} + 0.0219 \times 10^{-3}$ $k = -0.01719 (\sigma - p)^{-1.38} + 0.0219 \times 10^{-3}$ $k = -0.01719 (\sigma - p)^{-1.38} + 0.0219 \times 10^{-3}$ $k = -0.01719 (\sigma - p)^{-1.38} + 0.0219 \times 10^{-3}$ $k = -0.01719 (\sigma - p)^{-1.38} + 0.0219 \times 10^{-3}$ $k = -0.0179 (\sigma - p)^{-1.38} + 0.0219 \times 10^{-3}$ $k = -0.0179 (\sigma - p)^{-1.38} + 0.0219 \times 10^{-3}$ $k = -0.0179 (\sigma - p)^{-1.38} + 0.0219 \times 10^{-3}$ $k = -0.0179 (\sigma - p)^{-1.38} + 0.0219 \times 10^{-3}$ $k = -0.0179 (\sigma - p)^{-1.38} + 0.0219 \times 10^{-3}$ $k = -0.0179 (\sigma - p)^{-1.38} + 0.0219 \times 10^{-3}$ $k = -0.0179 (\sigma - p)^{-1.38} + 0.0219 \times 10^{-3}$ $k = -0.0179 (\sigma - p)^{-1.38} + 0.0219 \times 10^{-3}$ $k = -0.0179 (\sigma - p)^{-1.38} + 0.0219 \times 10^{-3}$ $k = -0.0179 (\sigma - p)^$ | Property (dimension) | Equation | References |
| $k = 2.38 \times 10^{-1} k (-p)^{-3.81} + 2.56 \times 10^{-3.1}$ $k = 4.393 \times 10^{-1} k (-p)^{-3.92} - 1.459 \times 10^{-3.9}$ $k = 7.887 \times 10^{-1} k (-p)^{-3.92} - 1.459 \times 10^{-3}$ $k = 7.887 \times 10^{-1} k (-p)^{-3.92} + 6.215 \times 10^{-3}$ $k = 1.396 \times 10^{-1} k (-p)^{-3.92} + 6.215 \times 10^{-3}$ $k = 0.1129 (-p)^{-3.92} + 6.215 \times 10^{-3}$ $k = 0.1129 (-p)^{-3.92} + 5.214 \times 10^{-4}$ $k = 0.01129 (-p)^{-3.92} + 1.2383 \times 10^{-3}$ $k = 1.238 \times 10^{-3} + 1.2383 \times 10^{-3} + 1.2383 \times 10^{-3}$ $k = 1.238 \times 10^{-3} + 1.2383 \times 10^{-3} + 1.2383 \times 10^{-3} + 1.2383 \times 10^{-3}$ $k = 1.239 \times 10^{-3} + 1.238 \times 10^{-3} + 1.238 \times 10^{-3}$ $k = 1.239 \times 10^{-3} + 1.238 \times 10^{-3} \times 10^{-3}$ $k = 1.239 \times 10^{-3} + 1.239 \times 10^{-3} \times 10^{-3}$ $k = 1.239 \times 10^{-3} + 1.239 \times 10^{-3} \times 10^{-3}$ $k = 1.239 \times 10^{-3} + 1.239 \times 10^{-3} \times 10^{-3}$ $k = 1.239 \times 10^{-3} \times 10^{-3} \times 10^{-3}$ $k = 1.$ | FD-I Permeability (m ²) | $k = 4.493 \times 10^{-20} (\sigma - p)^{-1.306} + 9.803 \times 10^{-23}$ | Badt et al. (2020) |
| $k = 7.85 \times 10^{-18} \text{ We}$ $k = 1.88 \times 10^{-18} \text{ Gr} - p^{-1.89} - 1.439 \times 10^{-29} \text{ Nus}$ $k = 1.368 \times 10^{-18} \text{ Gr} - p^{-1.89} + 6.205 \times 10^{-29} \text{ Nus}$ $k = 1.368 \times 10^{-18} \text{ Gr} + 6.205 \times 10^{-29} \text{ Nus}$ $k = 1.368 \times 10^{-18} \text{ Gr} + 2.202 \times 10^{-29} \text{ Nus}$ $k = 0.0102(\alpha - p)^{-4.215}$ $k = 0.0102(\alpha - p)^{-4.215} + 2.242 \times 10^{-4} \text{ Nus}$ $k = 0.01129(\alpha - p)^{-4.215} + 2.242 \times 10^{-4} \text{ Nus}$ $k = 0.01129(\alpha - p)^{-4.215} + 1.429 \times 10^{-4} \text{ Nus}$ $k = 0.01129(\alpha - p)^{-4.215} + 1.429 \times 10^{-4} \text{ Nus}$ $k = 0.01129(\alpha - p)^{-4.215} + 1.429 \times 10^{-4} \text{ Nus}$ $k = 0.01129(\alpha - p)^{-4.215} + 1.429 \times 10^{-4} \text{ Nus}$ $k = 0.01129(\alpha - p)^{-4.215} + 1.429 \times 10^{-4} \text{ Nus}$ $k = 0.01129(\alpha - p)^{-4.215} + 1.429 \times 10^{-4} \text{ Nus}$ $k = 0.01129(\alpha - p)^{-4.215} + 1.429 \times 10^{-4} \text{ Nus}$ $k = 0.01129(\alpha - p)^{-4.215} + 1.429 \times 10^{-4} \text{ Nus}$ $k = 0.01129(\alpha - p)^{-4.215} + 1.429 \times 10^{-4} \text{ Nus}$ $k = 0.01129(\alpha - p)^{-4.215} + 1.429 \times 10^{-4} \text{ Nus}$ $k = 0.01129(\alpha - p)^{-4.215} + 1.429 \times 10^{-4} \text{ Nus}$ $k = 0.01129(\alpha - p)^{-4.215} + 1.429 \times 10^{-4} \text{ Nus}$ $k = 0.01129(\alpha - p)^{-4.215} + 1.429 \times 10^{-4} \text{ Nus}$ $k = 0.01129(\alpha - p)^{-4.215} + 1.429 \times 10^{-4} \text{ Nus}$ $k = 0.01129(\alpha - p)^{-4.215} + 1.429 \times 10^{-4} \text{ Nus}$ $k = 0.01129(\alpha - p)^{-4.215} + 1.429 \times 10^{-4} \text{ Nus}$ $k = 0.01129(\alpha - p)^{-4.215} + 1.429 \times 10^{-4} \text{ Nus}$ $k = 0.01129(\alpha - p)^{-4.215} + 1.429 \times 10^{-4} \text{ Nus}$ $k = 0.01129(\alpha - p)^{-4.215} + 1.429 \times 10^{-4} \text{ Nus}$ $k = 0.01129(\alpha - p)^{-4.215} + 1.429 \times 10^{-4} \text{ Nus}$ $k = 0.01129(\alpha - p)^{-4.215} + 1.429 \times 10^{-4} \text{ Nus}$ $k = 0.01129(\alpha - p)^{-4.215} + 1.429 \times 10^{-4} \text{ Nus}$ $k = 0.01129(\alpha - p)^{-4.215} + 1.429 \times 10^{-4} \text{ Nus}$ $k = 0.01129(\alpha - p)^{-4.215} + 1.429 \times 10^{-4} \text{ Nus}$ $k = 0.01129(\alpha - p)^{-4.215} + 1.429 \times 10^{-4} \text{ Nus}$ $k = 0.01129(\alpha - p)^{-4.215} + 1.429 \times 10^{-4} \text{ Nus}$ $k = 0.01129(\alpha - p)^{-4.215} + 1.429 \times 10^{-4} \text{ Nus}$ $k = 0.01129(\alpha - p)^{-4.215} + 1.429 \times 10^{-4} \text{ Nus}$ $k = 0.01129(\alpha - p)^{-4.215} + 1.429 \times 10^{-4} \text{ Nus}$ | FD-i Permeability (m²) | $k = 2.58 \times 10^{-18} (\sigma - p)^{-2.315} + 2.56 \times 10^{-21}$ | Badt et al. (2020) |
| $k = 7.887 \times 10^{-18} (\sigma - p)^{-1887} + 0.10^{-20}$ $k = 1.398 \times 10^{-18} (\sigma - p)^{-1887} + 0.021 \times 10^{-20}$ $\phi = -9.702 \times 10^{-2} (\sigma - p)^{-1887} + 0.021 \times 10^{-20}$ $\theta = -9.702 \times 10^{-2} (\sigma - p)^{-1887} + 0.021 \times 10^{-2}$ $\phi = 0.01129 (\sigma - p)^{-1218}$ $\phi = 0.01129 (\sigma - p)^{-1218}$ $has be equal to the equal to t$ | FD-h Permeability (m²) | $k = 4.493 \times 10^{-18} (\sigma - p)^{-1.332} - 1.439 \times 10^{-20}$ | Badt et al. (2020) |
| $k = 1.396 \times 10^{-16} (a - p)^{-168} + 6.205 \times 10^{-20}$ $\phi = -9.702 \times 10^{-3} (-1004)$ $\phi = -0.1129 (a - p)^{-1619} + 0.004$ $\phi = 0.01129 (a - p)^{-1619} + 0.0229$ $h = -0.1139 (a - p)^{-1619} + 0.0229$ $h = -0.1029 \times 10^{-2} T + 2.039$ $h = -0.1029 \times 10^{-2} T + 1.039$ $h =$ | WG Permeability (m ²) | $k = 7.887 \times 10^{-18} (\sigma - p)^{-0.9837} - 1.021 \times 10^{-20}$ | Nasseri et al. (2009) |
| $\phi = -9.702 \times 10^{-3}e^{-6.0044} \qquad \text{BB}$ $\phi = 0.0129(a - p)^{-0.204} \qquad \text{Nas}$ $\phi = 0.01129(a - p)^{-0.004} + 0.4259 \qquad \text{Nas}$ $\phi = 0.01129(a - p)^{-0.004} + 0.4259 \qquad \text{Nas}$ $\phi = 0.01129(a - p)^{-0.004} + 0.4259 \qquad \text{O}$ $\phi = 0.01129(a - p)^{-0.004} $ | HG Permeability (m²) | $k = 1.396 \times 10^{-16} (\sigma - p)^{-1.665} + 6.205 \times 10^{-20}$ | N&S (2005) |
| $\phi = 0.0192(\sigma - p)^{-4.274} \qquad \text{BB}$ $\phi = 0.01129(\sigma - p)^{-4.274} \qquad \text{Nas}$ $\phi = 0.01129(\sigma - p)^{-4.274} \qquad \text{Nas}$ $\phi = 0.01129(\sigma - p)^{-4.274} \qquad \text{Nas}$ $\phi = 0.01129(\sigma - p)^{-4.274} \qquad \text{O}$ $\phi = 0.0129(\sigma - p)^{-4.274}$ | FD-1, FD-h Porosity | $\phi = -9.702 \times 10^{-3} k^{-0.03604} + 0.0604$ | Badt et al. (2020) |
| $\phi = 0.01129(\sigma - p)^{-0.037} + 5.274 \times 10^{-4}$ $\phi = -0.1719(\sigma - p)^{-0.037} + 5.274 \times 10^{-4}$ $\phi = -0.1719(\sigma - p)^{-0.037} + 0.4529$ $(-1.018)^{-1} + 0.4239$ $(-1.018)^{-1} + 0.233 \sin(0.382 \times 10^{-7} + 0.5628)$ $(-1.018)^{-1} + 0.233 \sin(0.382 \times 10^{-7} + 2.242)$ $(-1.023)^{-1} + 0.273 \sin(0.382 \times 10^{-7} + 2.242)$ $(-1.033)^{-1} + 0.274 \sin(0.382 \times 10^{-7} + 2.242)$ $(-1.033)^{-1} + 0.274 \sin(0.382 \times 10^{-7} + 2.242)$ $(-1.033)^{-1} + 0.233 \sin(0.382 \times 10^{-3} + 0.274 \times 10^{-3} + 0.$ | FD-i Porosity | $\phi = 0.0192(\sigma - p)^{-0.274}$ | Badt et al. (2020) |
| $\phi = -0.1719(\sigma - p)^{a_{1103}} + 0.4259$ $\rho_{r} = 902.4 \sin(2.859 \times 10^{-3} T + 0.5628)$ $+ 5.24 \sin(2.863 \times 10^{-3} T + 1.109)$ $+ 40.23 \sin(1.603 \times 10^{-3} T + 2.322)$ $+ 14.27 \sin(2.648 \times 10^{-3} T + 2.332)$ $+ 6.47 \sin(2.648 \times 10^{-3} T - 2.332)$ $+ 6.47 \sin(3.648 \times 10^{-3} T - 0.392)$ $+ 3.075 \sin(4.568 \times 10^{-3} T - 4.688)$ $\beta_{\rho} = \frac{(b_{\sigma} - b_{\rho})(b_{\sigma} + a_{\rho})}{b_{\sigma} + a_{\sigma}} - b_{\rho}$ Rer $p_{\mu} = \frac{(b_{\sigma} - b_{\rho})(b_{\sigma} + a_{\rho})}{b_{\sigma} + a_{\sigma}} - b_{\rho}$ $h_{\rho} = 10^{-18} T^{4} + 6 \times 10^{-14} T^{2} - 3 \times 10^{-12} T + 5 \times 10^{-10}$ $h_{\rho} = \frac{(b_{\sigma} - b_{\rho})(b_{\sigma} + a_{\rho})}{b_{\sigma} + a_{\sigma}} - b_{\sigma}$ $h_{\sigma} = \frac{(b_{\sigma} - b_{\rho})(b_{\sigma} + a_{\rho})}{b_{\sigma} + a_{\sigma}} - b_{\sigma}$ $h_{\sigma} = \frac{(b_{\sigma} - b_{\rho})(b_{\sigma} + a_{\rho})}{b_{\sigma} + a_{\sigma}} - b_{\sigma}$ $h_{\sigma} = \frac{(b_{\sigma} - b_{\rho})(b_{\sigma} + a_{\rho})}{b_{\sigma} + a_{\sigma}} - b_{\sigma}$ $h_{\sigma} = \frac{(b_{\sigma} - b_{\sigma})(b_{\sigma} + a_{\rho})}{b_{\sigma} + a_{\sigma}} - b_{\sigma}$ $h_{\sigma} = \frac{(b_{\sigma} - b_{\sigma})(b_{\sigma} + a_{\rho})}{b_{\sigma}} - b_{\sigma}$ $h_{\sigma} = \frac{(b_{\sigma} - a_{\sigma})(b_{\sigma} + a_{\rho})}{b_{\sigma}} - b_{\sigma}$ $h_{\sigma} = \frac{(b_{\sigma} - a_{\sigma})(a_{\sigma})(a_{\sigma})}{b_{\sigma}} - b_{\sigma}$ $h_{\sigma} = \frac{(b_{\sigma} - a_{\sigma})(a_{\sigma})(a_{\sigma})(a_{\sigma})}{b_{\sigma}} - b_{\sigma}$ $h_{\sigma} = \frac{(b_{\sigma} - a_{\sigma})(a_{\sigma})(a_{\sigma})(a_{\sigma})(a_{\sigma})}{b_{\sigma}} - b_{\sigma}$ $h_{\sigma} = \frac{(b_{\sigma} - a_{\sigma})(a_{\sigma})(a_{\sigma})(a_{\sigma})(a_{\sigma})(a_{\sigma})}{b_{\sigma}} - b_{\sigma}$ $h_{\sigma} = \frac{(b_{\sigma} - a_{\sigma})($ | WG Porosity | $\phi = 0.01129(\sigma - p)^{-0.2057} + 5.274 \times 10^{-4}$ | Nasseri et al. (2009) |
| $\begin{aligned} \rho_{p} &= 902.4 \sin(2.859 \times 10^{-3} T + 0.5628) \\ &+ 5.24 \sin(3.82 \times 10^{-3} T + 1.909) \\ &+ 4.54 \sin(3.82 \times 10^{-3} T + 1.909) \\ &+ 4.0.43 \sin(1.363 \times 10^{-3} T + 2.22) \\ &+ 4.14.27 \sin(2.68 \times 10^{-2} T - 2.352) \\ &+ 5.0.3 \sin(4.568 \times 10^{-2} T - 2.352) \\ &+ 5.0.3 \sin(4.568 \times 10^{-2} T - 4.688) \\ &+ 14.27 \sin(4.568 \times 10^{-2} T - 4.688) \\ &+ 3.0.75 \sin(4.568 \times 10^{-2} T - 4.688) \\ &+ 5.0.75 \sin(4.568 \times 10^{-2} T - 4.688) \\ &+ 6.1.45 \sin(4.568 \times 10^{-2} T - 4.688) \\ &+ 6.1.45 \sin(4.568 \times 10^{-2} T - 4.688) \\ &+ 6.1.45 \sin(4.568 \times 10^{-2} T - 4.688) \\ &+ 6.1.45 \sin(4.568 \times 10^{-3} \cos(4.568 \times 10^{-3} \sin(2.568 \times$ | HG Porosity | $\phi = -0.1719(\sigma - p)^{0.1013} + 0.4259$ | N&S (2005) |
| $\beta_{p} = 10^{-18} T^{4} - 4 \times 10^{-16} T^{5} + 6 \times 10^{-14} T^{2} - 3 \times 10^{-12} T + 5 \times 10^{-10}$ $\beta_{\phi} = \frac{(\rho_{\phi} - b_{\phi})(\rho_{\phi} + r_{\phi})}{\phi(1 + b\phi)} - \rho_{s}$ $h_{\text{FD,WG}} = 10, b_{\text{HG}} = 3$ $r = 1$ $- 1.67 \times 10^{-3} \text{ sin}(Tb)$ $- 1.63 \times 10^{-3} \text{ sin}(Tb)$ $- 1.63 \times 10^{-3} \text{ sin}(Tb)$ $- 1.68 \times 10^{-3} \text{ sin}(Tb)$ $- 1.66 \times 10^{-3} \text{ sin}(Tb)$ $- 1.408 \times 10^{-3} \text{ sin}(Tb)$ $+ 1.25 \times 10^{-4} \text{ sin}(Tb)$ $+ 2.25 \times 10^{-4} \text{ sin}(Tb)$ $+ 2.25 \times 10^{-4} \text{ sin}(Tb)$ $+ 2.25 \times 10^{-4} \text{ sin}(Tb)$ $+ 2.24 \times 10^{-4} \text{ sin}(Tb)$ $+ 2.04 \times 10^{-3} \text{ sin}(Tb)$ where $\nu = 4.688 \times 10^{-3}$ | Fluid density (kg/m³) for $25 \le T \le 1,040$ °C | $\rho_f = 902.4 \sin(2.859 \times 10^{-3} T + 0.5628) + 524 \sin(5.082 \times 10^{-3} T + 1.909) + 40.23 \sin(1.693 \times 10^{-2} T + 2.242) + 21.49 \sin(1.264 \times 10^{-2} T + 3.083) + 14.27 \sin(2.668 \times 10^{-2} T - 2.352) + 6.579 \sin(3.611 \times 10^{-2} T - 0.3007) + 3.075 \sin(4.568 \times 10^{-2} T - 4.688)$ | Calculated based on data from NIST (2022) for water at 50 MPa |
| $\beta_d = \beta_1(1 + b\phi)$ $\beta_\phi = \frac{(b_d - b_1)(b_d + b_2)}{\phi(1 + v)b_d} - \beta_s$ dio $b_{\text{ED,WG}} = 10. b_{\text{EG}} = 3$ $-1.673 \times 10^{-3} \sin(T\nu)$ $-1.673 \times 10^{-3} \sin(T\nu)$ $-1.408 \times 10^{-4} \cos(2T\nu)$ $-1.408 \times 10^{-3} \cos(3T\nu)$ $-1.408 \times 10^{-3} \sin(3T\nu)$ $-1.405 \times 10^{-3} \sin(3T\nu)$ $-1.405 \times 10^{-3} \sin(3T\nu)$ $-1.57 \times 10^{-3} \sin(3T\nu)$ $-1.57 \times 10^{-3} \sin(3T\nu)$ $+1.27 \times 10^{-4} \sin(7T\nu)$ $+8.64 \times 10^{-4} \sin(7T\nu)$ $+9.252 \times 10^{-4} \sin(6T\nu)$ $+2.04 \times 10^{-4} \sin(7T\nu)$ $+3.04 \times 10^{-3} \sin(8T\nu)$ where $\nu = 4.688 \times 10^{-3}$ | Fluid compressibility (Pa ⁻¹) | - 1 | NIST (2022) |
| $\beta_{\phi} = \frac{(h_d - h_s)(h_d + h_s)}{\phi(t + t + h)t_d} - \beta_s$ Idio $r = 1$ $r = 1$ $r = 1$ $- 1.673 \times 10^{-3} \sin(T_s)$ $- 1.673 \times 10^{-3} \sin(T_s)$ $- 1.673 \times 10^{-3} \sin(T_s)$ $- 1.408 \times 10^{-4} \cos(2T_s)$ $- 1.408 \times 10^{-3} \sin(3T_s)$ $- 1.408 \times 10^{-3} \sin(3T_s)$ $- 1.405 \times 10^{-3} \sin(3T_s)$ $- 1.405 \times 10^{-3} \sin(3T_s)$ $+ 1.257 \times 10^{-3} \sin(3T_s)$ $+ 1.257 \times 10^{-3} \sin(3T_s)$ $+ 1.257 \times 10^{-4} \sin(3T_s)$ $+ 1.257 \times 10^{-4} \sin(3T_s)$ $+ 2.24 \times 10^{-3} \sin(3T_s)$ $+ 2.24 \times 10^{-4} \sin(3T_s)$ $+ 2$ | Drained compressibility (Pa ⁻¹) | $eta_d = eta_s(1+b\phi)$ | Renner et al. (2000) |
| atio | Pore space compressibility (Pa ⁻¹) | $eta_{\phi} = rac{(eta_d - eta_s)(eta_d + reta_s)}{\phi_d(1 + reta_d)} - eta_s$ | Rice (2006) |
| atio $r = 1$ $\alpha_f = 3.652 \times 10^{-3} + 1.133 \times 10^{-3} \cos(T\nu)$ $-1.673 \times 10^{-3} \sin(T\nu)$ $-1.628 \times 10^{-4} \cos(2T\nu)$ $-4.084 \times 10^{-3} \sin(2T\nu)$ $-1.665 \times 10^{-3} \cos(3T\nu)$ $-1.665 \times 10^{-3} \sin(3T\nu)$ $-1.665 \times 10^{-3} \sin(3T\nu)$ $-1.405 \times 10^{-3} \sin(3T\nu)$ $-2.331 \times 10^{-3} \cos(4T\nu)$ $+1.257 \times 10^{-4} \cos(5T\nu)$ $+2.24 \times 10^{-4} \cos(5T\nu)$ $+2.24 \times 10^{-4} \cos(7T\nu)$ $+2.24 \times 10^{-4} \cos(7T\nu)$ $+2.044 \times 10^{-4} \cos(7T\nu)$ | Porosity factor b (in β_d expression) | $b_{\rm FD,WG} = 10, b_{\rm HG} = 3$ | Renner et al. (2000) |
| $\alpha_{f} = 3.652 \times 10^{-3} + 1.133 \times 10^{-3} \cos(T\nu)$ $- 1.673 \times 10^{-3} \sin(T\nu)$ $- 1.428 \times 10^{-4} \sin(T\nu)$ $- 4.084 \times 10^{-3} \sin(2T\nu)$ $- 1.665 \times 10^{-3} \cos(3T\nu)$ $- 1.405 \times 10^{-3} \sin(3T\nu)$ $- 1.405 \times 10^{-3} \sin(3T\nu)$ $- 1.405 \times 10^{-3} \sin(3T\nu)$ $- 1.257 \times 10^{-4} \sin(4T\nu)$ $+ 1.257 \times 10^{-4} \sin(6T\nu)$ $+ 8.64 \times 10^{-4} \cos(5T\nu)$ $+ 9.252 \times 10^{-4} \sin(6T\nu)$ $+ 2.24 \times 10^{-4} \cos(6T\nu)$ $+ 2.04 \times 10^{-4} \cos(8T\nu)$ $+ 2.044 \times 10^{-4} \cos(8T\nu)$ $- 3.114 \times 10^{-5} \sin(8T\nu)$ where $\nu = 4.688 \times 10^{-3}$ | r-Function of drained Poisson's ratio | r = 1 | B&M (2018) |
| | Fluid thermal expansivity (°C ⁻¹) | $a_f = 3.652 \times 10^{-3} + 1.133 \times 10^{-3} \cos(T\nu)$ $-1.673 \times 10^{-3} \sin(T\nu)$ $-1.428 \times 10^{-4} \cos(2T\nu)$ $-4.084 \times 10^{-3} \sin(2T\nu)$ $-1.655 \times 10^{-3} \sin(3T\nu)$ $-1.405 \times 10^{-3} \sin(3T\nu)$ $-2.331 \times 10^{-3} \sin(3T\nu)$ $+1.257 \times 10^{-4} \sin(4T\nu)$ $-7.524 \times 10^{-4} \sin(5T\nu)$ $+8.64 \times 10^{-4} \sin(5T\nu)$ $+7.29 \times 10^{-5} \cos(6T\nu)$ $+9.252 \times 10^{-4} \sin(7T\nu)$ $+2.01 \times 10^{-4} \sin(7T\nu)$ $+2.014 \times 10^{-4} \sin(7T\nu)$ $+2.014 \times 10^{-4} \sin(8T\nu)$ where $\nu = 4.688 \times 10^{-3}$ | Calculated from isobaric water volume data at 50 MPa from NIST (2022) |

| Continued | | |
|---|---|----------------------|
| Property (dimension) | Equation | References |
| Dynamic viscosity of fluid (Pa-s) for $T \le 600^{\circ}$ C | $\eta = 8.725 \times 10^{-29} T^9 - 4.171 \times 10^{-25} T^8$ $+ 7.819 \times 10^{-22} T^7$ $- 6.767 \times 10^{-19} T^6$ $+ 1.678 \times 10^{-16} T^5$ $+ 1.687 \times 10^{-13} T^4$ $- 1.608 \times 10^{-13} T^3$ $+ 5.859 \times 10^{-8} T^2 - 1.056 \times 10^{-5} T$ $+ 9.106 \times 10^{-4}$ | NIST (2022) |
| Dynamic viscosity of fluid (Pa-s) for $T > 600^{\circ}$ C | $\eta = 3.553 \times 10^{-5}$ | NIST (2022) |
| Pore space thermal expansivity (°C-1) | $\phi^{\wp} = {}^{\phi} x$ | |
| Thermal conductivity (W m ⁻¹ °C ⁻¹) | $K = \phi K_f + (1 - \phi)K_s$ | |
| Storage capacity (Pa ⁻¹) | $S = \phi(\beta_f + \beta_\phi)$ | Rice (2006) |
| Thermal expansivity of solid (°C ⁻¹) | $\alpha_s = -10^{-7}$ | Rice (2006) |
| Compressibility of solid (Pa ⁻¹) | $\beta_s = 2 \times 10^{-11}$ | B&M (2018) |
| Thermal conductivity of solid (W m $^{-1}$ $^{\circ}C^{-1}$) | $K_{\mathrm{FD,WG}} = 2$ | Robertson (1988) |
| | $K_{\rm HG} = 2.07$ | N&S (2005) |
| Thermal conductivity of fluid (W m ⁻¹ °C ⁻¹) | $K_f = 0.64$ | NIST (2022) |
| Heat capacity of rock (J kg $^{-1}$ $^{\circ}$ C $^{-1}$) | $c_{\text{FD}} = 627.6$ | Robertson (1988) |
| | $c_{\rm WG} = 900$ | Robertson (1988) |
| | $c_{\rm HG} = 1,180$ | N&S (2005) |
| Friction coefficient | $\mu_{\mathrm{FD}} = 0.9$ | Badt et al. (2020) |
| | $\mu_{ m WG}=0.6$ | Beeler et al. (1996) |
| | $\mu_{\mathrm{HG}} = 0.4$ | N&S (2005) |

Note. Fredrick diabase (FD): low permeability (FD-1), intermediate permeability (FD-i) and high permeability (FD-h); Westerly granite (WG); Hanaore fault gouge (HG); N&S (2005) = Noda and Shimamoto (2005); B&M (2018) = Brantut and Mitchell (2018). All effective stress expressions ($\sigma - p$) are in units of MPa.

Figure 2. Model geometry: the fault plane is depicted by a heavy horizontal line at x = 0, model nodes (indexed by n, from 1 to N) are evenly spaced between $0 \le x \le L$ at Δx . The fault slips at a constant velocity v.

and density of the pore fluid remain in the spatial derivative in Equation 3. The latter two make Equations 2 and 3 non-linear and are solved numerically with flux-conservative derivatives.

2.3. Model Setup

The model is run assuming that slip is localized along the fault plane at x=0, where x increases in the direction normal to the fault plane (Figure 2). All simulations start with uniform pore pressure $p_0=25$ MPa and temperature $T_0=75$ °C, corresponding to a seismogenic depth of 2.5 km (e.g., Scholz, 2002). We chose this depth so that pore pressure remains above the critical point (NIST, 2022), thus preventing the phase transition of water from liquid to a gas, as in previous experimental studies of TP (Acosta

et al., 2018; Badt et al., 2020; Yao et al., 2023). The model boundary at x = L allows heat and fluid-mass flux across, while, due to the symmetry of the model, fluid and heat transport is zero across the fault plane (x = 0). The distance L is chosen to be large enough that the pore pressure and temperature remain unchanged throughout the simulation at x = L (and thus the heat and fluid mass fluxes across this boundary are zero as well). L is specified for each simulated fault rock type, where L equals to 1.5 mm, 2 and 5 mm for low, intermediate and high permeability diabase, respectively, 12 mm for Westerly granite and 5 mm for Hanaore Fault gouge. The grid spacing Δx is uniform in the model (and equal to 10^{-6} m) and thus the number of grid nodes is calculated as $N = L/\Delta x$. Heat production is introduced as a boundary condition at the fault plane, where the heat production per unit fault area caused by friction at the ith timestep q_i^t is estimated with:

$$q_h^i = \frac{1}{2}\mu(\sigma - p_1^i)v,\tag{11}$$

where the subscript denotes the node number (n = 1, Figure 2). We use an adaptive timestep Δt^i that satisfies the numerical stability condition (Equation 12) based on the greatest calculated diffusivity (thermal κ or hydraulic ω) in the grid-space from the previous timestep:

$$\Delta t^{i+1} = \frac{\Delta x^2}{3 \max\{\kappa_n^i, \omega_n^i\}} \,. \tag{12}$$

During each simulation, we compute the width of the pressurized zone h, defined as the distance away from the fault plane where the pore fluid pressure satisfies:

$$\frac{p}{\sigma} \ge 0.75. \tag{13}$$

The threshold of 0.75 is arbitrary, though the results (Figure 14) are qualitatively robust with respect to this arbitrary value. The pressurized zone width is always smaller than the model domain length *L*. This metric is important when considering the effects of TP on realistic fault zone structure. Because the hydraulic structure of localized faults consists of a low permeability core surrounded by a fractured (and thus more permeable) damage zone (e.g., Faulkner et al., 2010; Wibberley & Shimamoto, 2003), weakening by TP may be inhibited by the change in drainage regime when the zone of over pressurized fluid (pressurized fluid above its ambient pressure) overlaps the damage zone.

2.4. Convergence of the Numerical Solution

Numerical errors for the constant TP case are quantified by comparing the analytical solution for temperature (Equation 7) and pore pressure (Equation 8) to the numerical solution at the fault plane (x = 0). The errors vary with time t and grid spacing Δx . The numerical errors in temperature and pore pressure (over time) are calculated as:

$$\begin{cases} \operatorname{Err}_{T} = \frac{\sqrt{\left(T_{\operatorname{anl}}^{i} - T_{n=1,\operatorname{num}}^{i}\right)^{2}}}{T_{\operatorname{anl}}^{i}} \\ \operatorname{Err}_{p} = \frac{\sqrt{\left(p_{\operatorname{anl}}^{i} - p_{n=1,\operatorname{num}}^{i}\right)^{2}}}{p_{\operatorname{anl}}^{i}}, \end{cases}$$
(14)

BADT ET AL. 7 of 22

21699356, 2023, 8, Downloaded from https://agupubs.onlinelibrary.wiley.com/doi/10.1029/2023JB026558 by Brown University Library, Wiley Online Library on [31/08/2023]. See

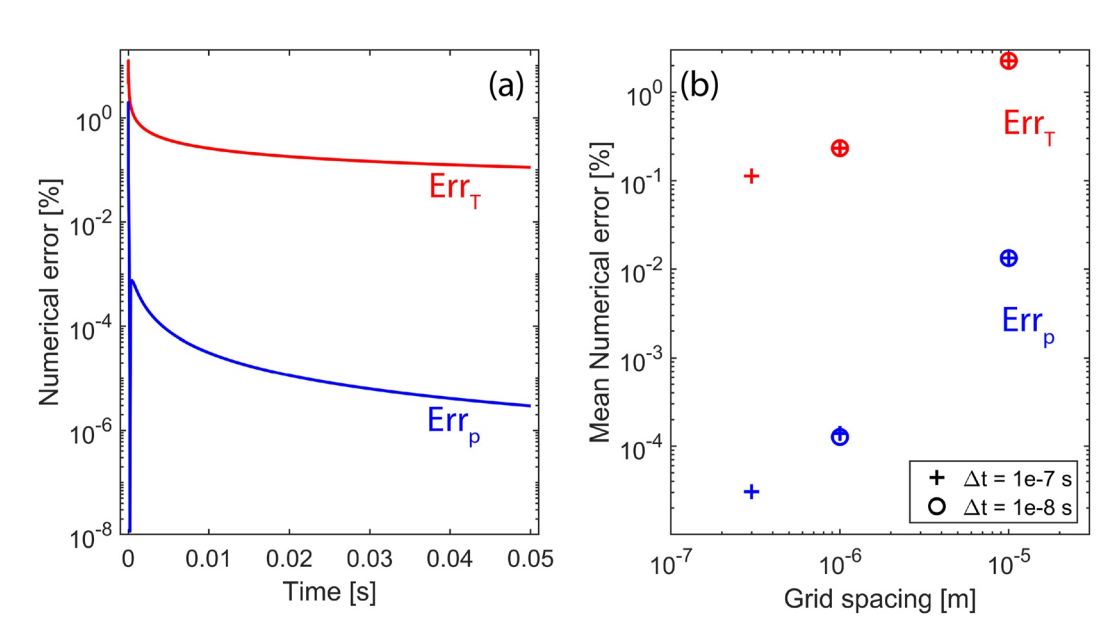


Figure 3. Calculated numerical errors for temperature (Err_T in red) and pore pressure (Err_p in blue). (a) Numerical errors versus time for a simulation with a grid spacing of $\Delta x = 10^{-6}$ m. (b) Mean numerical errors (averaged over time) for various simulations with varying grid spacing and timestep sizes.

where the subscripts and num denote analytical solution and numerical solution, respectively. The errors at each timestep i are normalized by the analytical temperature (for Err_T) and pore pressure (for Err_p) at the same timestep.

Figure 3a presents the numerical errors for temperature (Err_T) and pore pressure (Err_p) over time for a simulation with a grid spacing of $\Delta x = 10^{-6}$ m, as in all simulations conducted in this study. The maximum temperature error of 12% (~4°C) and maximum pore pressure error of 2% (~0.5 MPa) are high but decrease significantly with time, where $Err_T < 0.1\%$ after 10^{-3} s and $Err_p < 0.1\%$ after 10^{-6} s. In general, the numerical errors are negligible after the very early stages of fault slip ($\delta > 1$ mm). Figure 3b presents results of the mean numerical errors (averaged over the simulated time per simulation) in temperature and pore pressure for different grid spacing and time step sizes. The mean numerical errors for a simulation with grid spacing of 10^{-6} m are ~0.2% and 0.0001% for the temperature and pore pressure, respectively. The timestep size has a second-ordered effect on the errors as expected from the truncation error of the centered scheme. In general, the adaptive timestep size in all simulations reported here are smaller than 3×10^{-7} s. In addition, the numerical errors are also affected by the simulated slip velocity, where the errors decrease with a decrease in modeled slip velocity (Supporting Information S1). The largest numerical errors, specifically for temperature, in the beginning of the simulations are mainly due to the large thermal gradients when the temperature increases significantly due to the high initial shear stress.

Overall, the numerical errors are not expected to change the temperature prediction by the variable case model in a meaningful way and are strongly affected by the large temperature gradients in the very early stages. At the early stage in the simulations the difference between the constant and variable cases is of the same order as the numerical error. It is only later in the simulation (simulated time >0.005 s) that the difference between the constant case and the variable case become increasingly large, which corresponds to numerical error in the temperature calculation $\text{Err}_T < 0.1\%$.

2.5. Material Properties

Parameter values for the studied rocks and for the pore fluid—water, are summarized in Table 1. Porosity is the main parameter that controls other important poroelastic and thermal properties, such as the pore space compressibility β_{ϕ} and bulk thermal conductivity K (Table 1); it also deeply related to permeability k (e.g., Bernabé et al., 2003). The variations of permeability and porosity with effective stress are plotted in Figure 4 for the Frederick diabase (FD) from Badt et al. (2020), thermally-cracked Westerly granite (at 650°C) from Nasseri et al. (2009) and for clay-rich gouge from the Hanaore fault from Noda and Shimamoto (2005). The FD data include three sets of permeability values: low, intermediate, and high. Badt et al. (2020) varied the hydraulic properties of their diabase specimens by applying different heat treatment protocols, which led to different

BADT ET AL. 8 of 22

onlinelibrary.wiley.com/doi/10.1029/2023JB026558 by Brown University Library

ns) on Wiley Online Library for rules of use; OA articles are governed by the applicable Creat

Figure 4. Permeability (a) and porosity (b) versus effective stress for Frederick diabase (FD, blue curves), Westerly granite (red curve) and Hanaore fault gouge (black curve). For FD, the dashed line depicts low permeability, dash-dotted line depicts intermediate permeability and solid line depicts high permeability.

amounts of microscopic thermal cracking (Fredrich & Wong, 1986). Porosity-effective stress data for the diabase are available only for the intermediate permeability. We estimated the porosity-effective stress relationships for the high and low permeability diabase by assuming that the samples follow the same permeability-porosity relationship as the intermediate permeability diabase.

The pressurization factor Λ controls fluid pressurization in the model (Rice, 2006). Equation 4 describes Λ as derived by Rice (2006) and its components are summarized in Table 1. The pressurization factor is a function of both pore pressure, through the dependence of the pore space compressibility β_{ϕ} and thermal expansivity α_{ϕ} on porosity, and temperature, through the fluid compressibility β_{f} and thermal expansivity α_{f} (Table 1). Figure 5 illustrates the isobaric behavior of the pressurization factor, as calculated for intermediate permeability FD (Figures 5a and 5b), Westerly granite and Hanaore fault gouge (Figure 5b). Λ is predominantly a function of temperature at these conditions, where Figure 5a demonstrates that the effects of pressure are negligible relative to the effects of temperature.

The pressurization factor is greatest around 200°C, above which it decreases with temperature (Figure 5) for all three rock types—Frederick diabase, Westerly granite and Hanaore fault gouge. The increase in Λ with temperature (up to ~200°C) and then decrease with temperature is explained by examining the individual components of Λ and their evolution at this temperature range (25–600°C) and fluid pressure range (25–71.25 MPa). Figure 6 depicts the evolution of the thermal expansivity, which makes up the numerator of Λ (Equation 4), and compressibility, which makes up the denominator of Λ , with temperature. The thermal expansivity difference ($\alpha_c - \alpha_d$) is

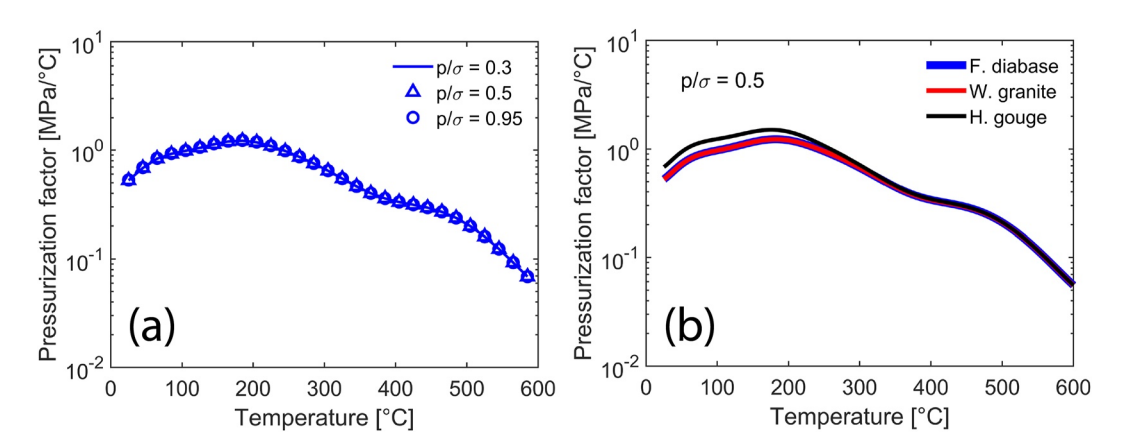


Figure 5. Isobaric variations of the pressurization factor with temperature for Frederick diabase (FD) (a) and for FD, Westerly granite and Hanaore fault gouge (b). The calculations for the diabase were based on the porosity-effective stress relation for the intermediate permeability diabase. The effects of pressure are negligible, where calculations for different pore pressures (normalized by the normal stress, p/σ) collapse onto one curve (a). This observation is robust and pertains to all the lithologies considered here.

BADT ET AL. 9 of 22

21699356, 2023, 8, Downloaded from https://agupubs.onlinelibrary.wiley.com/doi/10.1029/2023JB026558 by Brown University Library, Wiley Online Library on [31/08/2023]

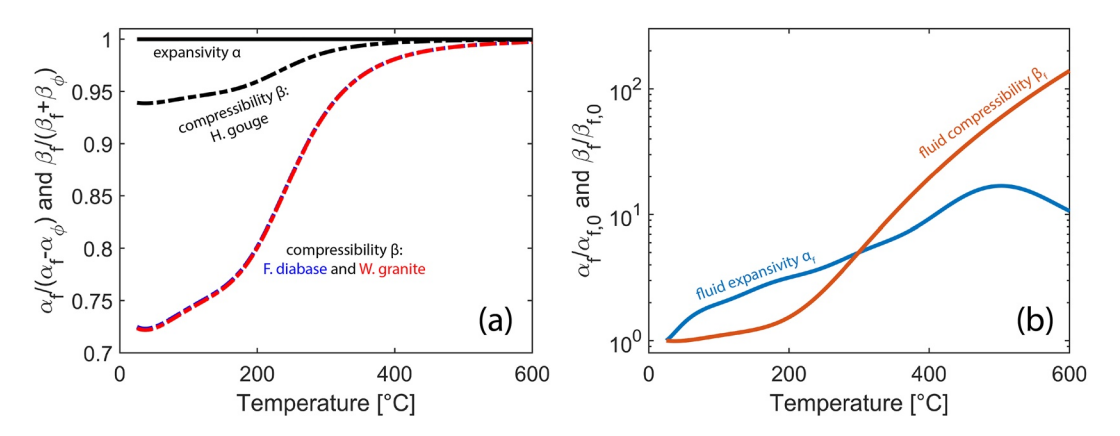


Figure 6. Variations of thermal expansivity (α) and compressibility (β) with temperature showing the importance of fluid properties as temperature increases. (a) Fluid expansivity (normalized by the numerator of Λ —solid lines) and compressibility (normalized by the denominator of Λ —dashed lines). The expansivity for all three rock types collapse into one curve (the black solid line) and is effectively controlled by the fluid expansivity α_f (b) Variations of fluid expansivity and compressibility (normalized by their initial value, respectively) with temperature.

controlled entirely by the fluid expansivity α_f , as $\alpha_f(\alpha_f - \alpha_\phi) \approx 1$ over the specified temperature range (Figure 6a—solid line). The sum of fluid and pore space compressibility ($\beta_f + \beta_\phi$) becomes increasingly controlled by fluid compressibility β_f as temperature increases (Figure 6a—dashed lines). Altogether this means that Λ becomes increasingly controlled by the fluid properties at higher temperatures ($\geq 400^{\circ}$ C). Considering the less porous rocks, granite and diabase for which most of the porosity is made of cracks, fluid compressibility becomes increasingly dominant at temperatures >200°C. Whereas for the more porous rock, the Hanaore fault gouge, with an initial porosity of 17%, Λ is also controlled by the fluid properties at lower temperatures ($<400^{\circ}$ C). Figure 6b depicts the evolution of fluid expansivity and compressibility with temperature. At low temperatures ($\le200^{\circ}$ C) fluid expansivity increases more rapidly than the compressibility, which results in an overall increase in Λ . When the temperature exceeds roughly 200°C the fluid becomes increasingly compressible (even though fluid expansivity continues to increase with temperature), as it approaches the temperature where it transitions to supercritical fluid, 374°C (NIST, 2022). This behavior explains the continuous decrease in Λ with temperature as $T > 200^{\circ}$ C.

3. Results

We present four sets of simulations. *First*, we present a comparison of the constant hydraulic and thermal parameters model (the constant case) with Rice's (2006) analytical solution. *Second*, we contrast results obtained with the constant case and variable case models for intermediate permeability FD. *Third*, we explore the effects of varying the initial permeability of the diabase in the variable case model. *Fourth*, we extend our results using physical properties determined for Westerly granite and the Hanaore fault gouge. All simulations are run with constant normal stress on the fault plane ($\sigma = 75$ MPa), constant fault slip velocity (v = 1 m/s) and are stopped when the total displacement reaches 0.05 m. Initial conditions for all simulations are the same, with an initial pore pressure ($p_0 = 25$ MPa) and temperature ($T_0 = 75$ °C) homogenously distributed across the modeled fault zone. The choice to stop these simulations after a fault slip distance of 0.05 m was made so that the majority of fluid pressurization and frictional weakening is captured while also keeping the simulation computationally efficient. The fault slip in the results section is normalized by the length scale L^* (Equation 9). Because the diffusivities evolve in the variable case during a course of a simulation we define the normalization lengths scale to be L_0^* , which is Rice's (2006) L^* with diffusivities and Λ set to their initial values:

$$L_0^* = \frac{4}{\mu^2} \left(\frac{\rho c}{\Lambda_0}\right)^2 \frac{\left(\sqrt{\omega_0} + \sqrt{\kappa_0}\right)^2}{v} \tag{15}$$

3.1. The Constant Case Versus the Analytical Solution

The results of the numerical model compare well with the analytical solution by Rice (2006) given in Equations 7 and 8. Figure 7 shows the comparison of the numerical model solved with constant hydraulic and thermal

BADT ET AL. 10 of 22

onlinelibrary.wiley.com/doi/10.1029/2023JB026558 by Brown University Library

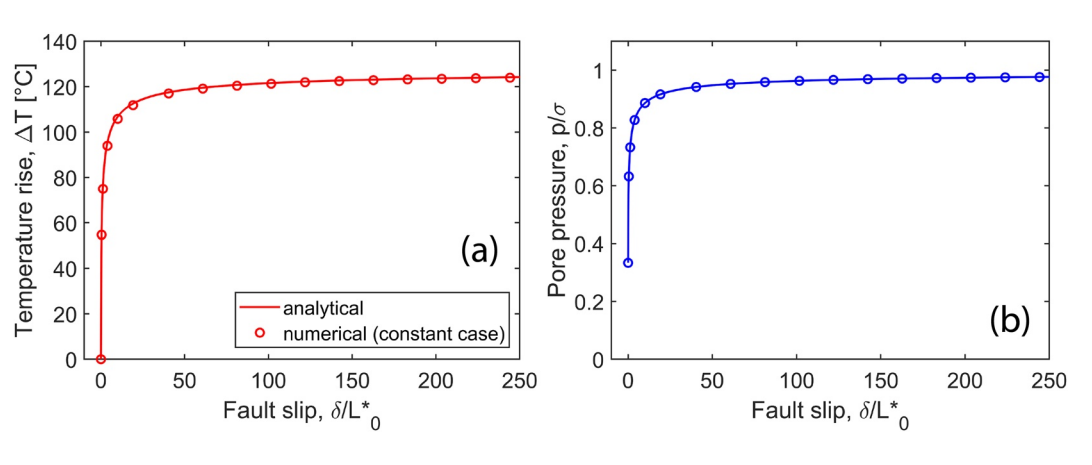


Figure 7. Temperature rise (a) and pore pressure (b) at the fault plane versus fault slip. Rice's (2006) analytical solution is depicted by a solid line, numerical solution for the constant case is depicted by open circles.

properties with Rice's (2006) analytical solution. This analysis was done for the intermediate permeability FD with a permeability of 2.86×10^{-21} m². The length scale L^* (Equation 9), defined by Rice (2006), is equal to 1.2275×10^{-4} m. This parameter is used in the analytical model calculations presented in Figure 7. In the constant case, the permeability, as do all other hydraulic and thermal properties, remains constant throughout the simulation. The convergence of the numerical solution to the analytical solution is robust with respect to all other rock types considered in this study. The mean numerical errors (over the simulation time) for temperature and pore pressure are 0.3° C and 7.6×10^{-5} MPa, respectively (Figure 7).

3.2. The Constant Versus Variable Cases

Figure 8 presents results from numerical simulations for the constant case (Figure 8, panels a, c, e, and g) and the variable case (Figure 8, panels b, d, f, and h) for the intermediate permeability diabase. All of the physical, hydraulic and thermal properties are initially identical for the two sets of simulations. The temperature rise ($\Delta T = T - T_0$, where $T_0 = 75$ °C) distribution in the fault zone is presented in Figures 8a and 8b for the constant and variable cases, respectively. The spatiotemporal distribution of temperature is similar between the two cases, though ΔT by the end of the simulation ($\delta/\delta_{\rm tot} = 1$) at the fault plane is slightly greater for the variable case, 133°C, versus 125°C in the constant case. This result correlates with the slightly lower pore pressure (normalized by the normal stress, p/σ) in the variable case, 0.979, versus the constant case, 0.981, by the end of the simulation. The shear stress varies directly with the pore pressure through Equation 1, where lower shear stress corresponds to higher pore pressure.

The difference between the constant and variable cases is most easily shown by the spatiotemporal distribution of pore pressure (Figures 8c and 8d), hydraulic diffusivity (Figures 8e and 8f) and the pressurization factor (Figures 8g and 8h). *First*, elevated pore pressures ($p/\sigma > 0.33$) extend further away from the fault plane in the *variable case* simulation; where high pore pressures ($p/\sigma > 0.75$) reach distances up to 1.1 mm, compared to 0.5 mm in the *constant case* simulation (Figures 8c and 8d). *Second*, hydraulic diffusivity (ω) evolves considerably in the fault zone during TP in the *variable case* (Figure 8f). For example, by the end of the simulation $\omega = 4.2 \times 10^{-4}$ m²/s at the fault plane, an increase by more than two orders of magnitude from its initial value $\omega_0 = 1.74 \times 10^{-6}$ m²/s. *Third*, the pressurization factor (Λ) changes during the *variable* case simulation in the fault zone where both temperature and pore pressure change, up to a distance of $x/L_0^* = 8$ from the fault plane (Figure 8h). Λ displays an initial increase near and at the fault plane, but this trend transitions to a continuous decrease after the fault slips ~3 mm ($\delta/\delta_{tot} = 0.06$). This transition is attributed to the temperature rise in this zone; where Λ decreases at T > 200°C (corresponding to $\Delta T > 125$ °C), as shown in Figure 5a. The maximum value of Λ is a factor of ~1.4 greater than its initial value ($\Lambda_0 = 0.886$ MPa/°C). The peak value of Λ moves away from the fault plane with time (Figure 8h inset) as the temperature increases with time (or slip) further away from the fault plane.

The comparison between the constant and variable cases shows that the spatiotemporal distribution of two key parameters that control TP, hydraulic diffusivity and fluid pressurization factor, can become significantly variable in a fault zone where TP is active. The effects of variable parameters are further emphasized by the distribution

BADT ET AL.

21699356, 2023, 8, Downloaded from https://agupubs.onlinelibrary.wiley.com/doi/10.1029/2023JB02658 by Brown University Library, Wiley Online Library on [31/08/2023]. See the Terms and Conditions (https://onlinelibrary.wiley.com/doi/10.1029/2023JB02658 by Brown University Library.

ons) on Wiley Online Library for rules of use; OA articles are governed by the applicable Creative

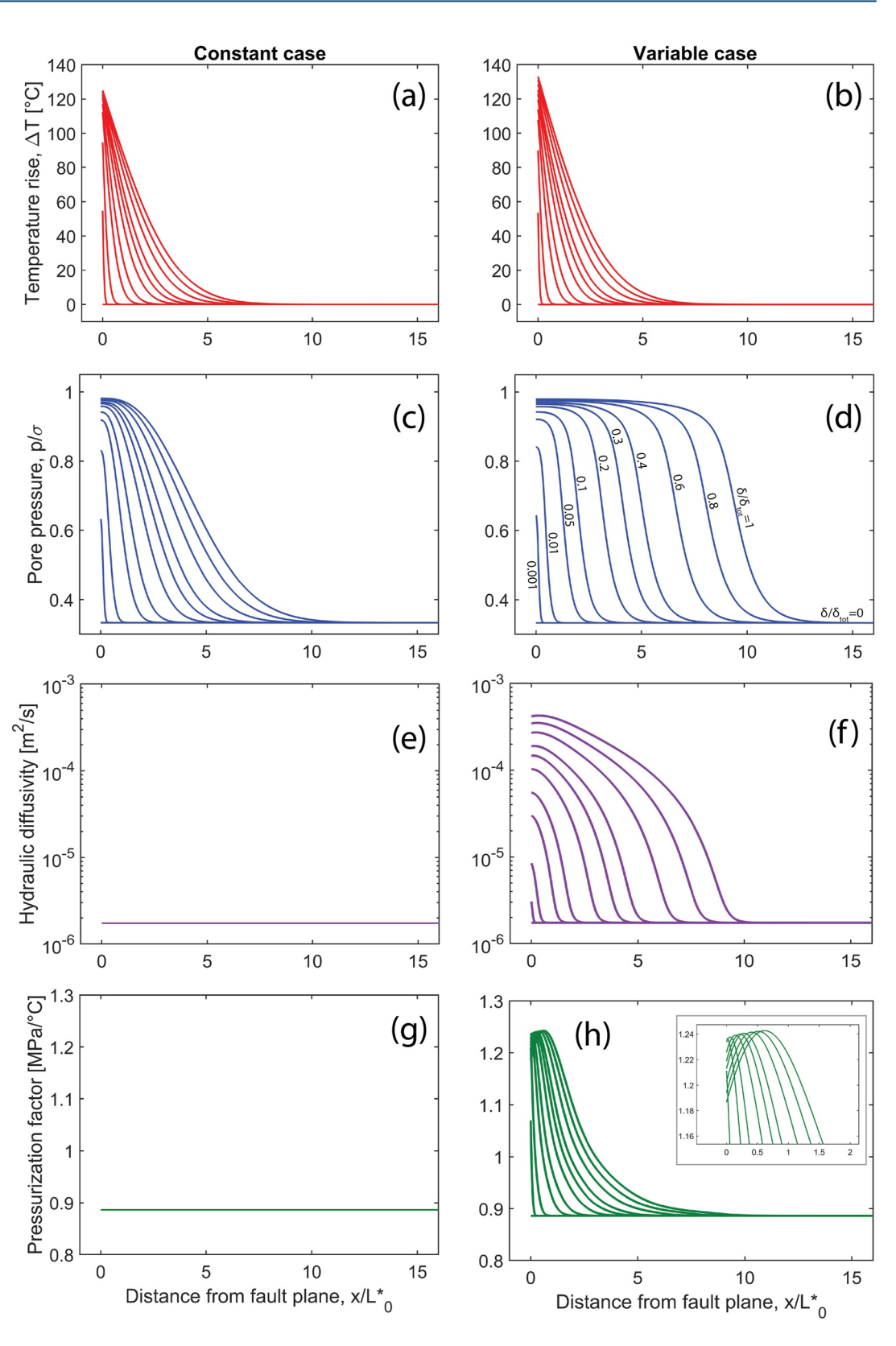


Figure 8. Temperature rise (a–b), pore pressure (c–d), hydraulic diffusivity (e–f) and pressurization factor (g–h) profiles for the two numerical models for the intermediate permeability diabase: constant case (left column) and variable case (right column). Each profile represents a snapshot at a different fault displacement (or time), as labeled in panel (d). Total displacement $\delta_{tot} = 50$ mm for these simulations. The inset in panel (h) is a blowup of the region close to the fault plane.

BADT ET AL. 12 of 22

nlinelibrary.wiley.com/doi/10.1029/2023JB026558 by Brown University Library, Wiley Online Library on [31/08/2023]. See the

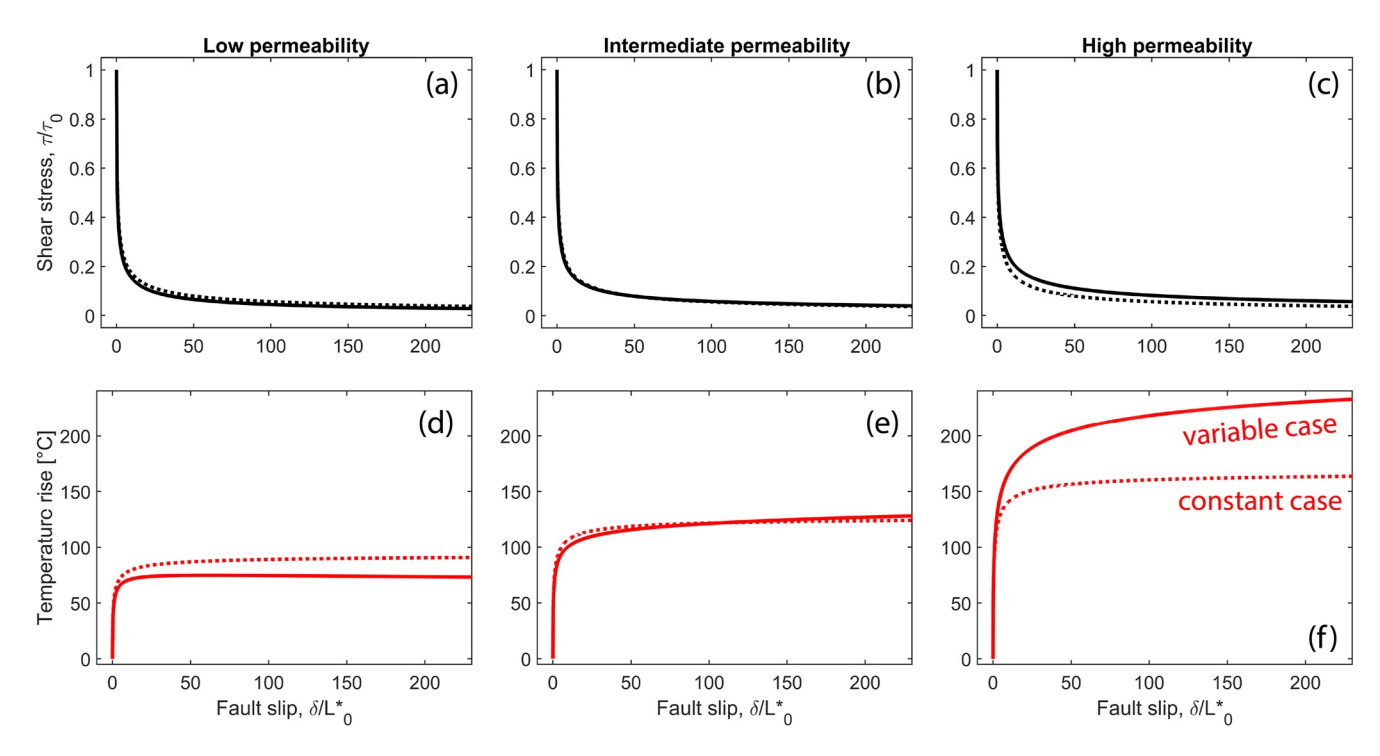


Figure 9. Shear stress (a–c) and temperature rise (d–f) at the fault plane versus fault slip for Frederick diabase with different starting permeability (k_0) : low $(k_0 \sim 10^{-22} \text{ m}^2)$, intermediate $(k_0 \sim 10^{-21} \text{ m}^2)$ and high $(k_0 \sim 10^{-20} \text{ m}^2)$. Solid lines and dotted lines represent variable and constant cases respectively.

of elevated pore pressure in the fault zone, in comparison to the *constant case*. While the shear stress and temperature rise on the fault plane are comparable between the two cases for the intermediate permeability diabase, we will show next that considering the *variable* case in TP calculations is crucial to the evolution of the hydraulic and poroelastic parameters of the fault zone materials.

3.3. The Effect of Initial Permeability in the Variable Case TP

Permeability (k) is a key parameter that controls hydraulic diffusion, and subsequently fluid pressurization and temperature rise in the fault zone (Equations 2 and 3). Porosity (ϕ) is closely related to permeability as an increase in porosity leads to a non-linear increase in permeability (e.g., Wang, 2017). In this section, we present results for the mechanical, thermal and hydraulic response of the fault plane for simulations using different initial permeability based on the values shown for FD in Figure 4. Initial porosity is also varied, though the permeability differences between the simulations in this section are greater than the porosity differences. TP simulations for FD of different permeability and porosity are considered: (a) low permeability—with initial permeability $k_0 = 2.43 \times 10^{-22}$ m² and initial porosity $\phi_0 = 0.21\%$; (b) intermediate permeability, where $k_0 = 2.86 \times 10^{-21}$ m² and $\phi_0 = 0.66\%$; and (c) high permeability, where $k_0 = 1.01 \times 10^{-20}$ m² and $\phi_0 = 0.94\%$. For these simulations all parameters in the model are identical except the permeability-effective stress and porosity-effective stress relations (Figure 4 and Table 1).

Figure 9 shows the results for shear stress, normalized by initial shear stress $\tau_0 = \mu(\sigma - p_0)$, and temperature rise (ΔT) evolution at the fault plane during TP. In general, the constant case shows similar, near complete, shear stress drops (or simply, stress drops, $\Delta \tau/\tau_0 = (\tau_0 - \tau_{\rm final})/\tau_0)$ as in the variable case for all three starting permeabilities. Closer examination of the results reveals that the constant case predicts a smaller stress drop, compared to the variable case, for the low permeability diabase, and a greater stress drop in the intermediate and high permeability diabase simulations (Figures 9a–9c). The difference in stress drop between the constant and variable cases becomes clearer in the high permeability diabase simulation (Figure 9c). The difference between the constant and variable cases is observed more easily in the temperature rise calculations (Figures 9d–9f). The low permeability simulation shows that for $\delta/L_0^* \geq 200 \ \Delta T = 73^{\circ}$ C in the variable case, compared to $\Delta T = 91^{\circ}$ C in the constant case (Figure 9d). In fact, ΔT in the variable case reaches its peak of 75°C at $\delta/L_0^* \sim 60$, after which it decreases gradually with continued slip. This temperature transition is completely absent in the constant case and is a result

BADT ET AL. 13 of 22



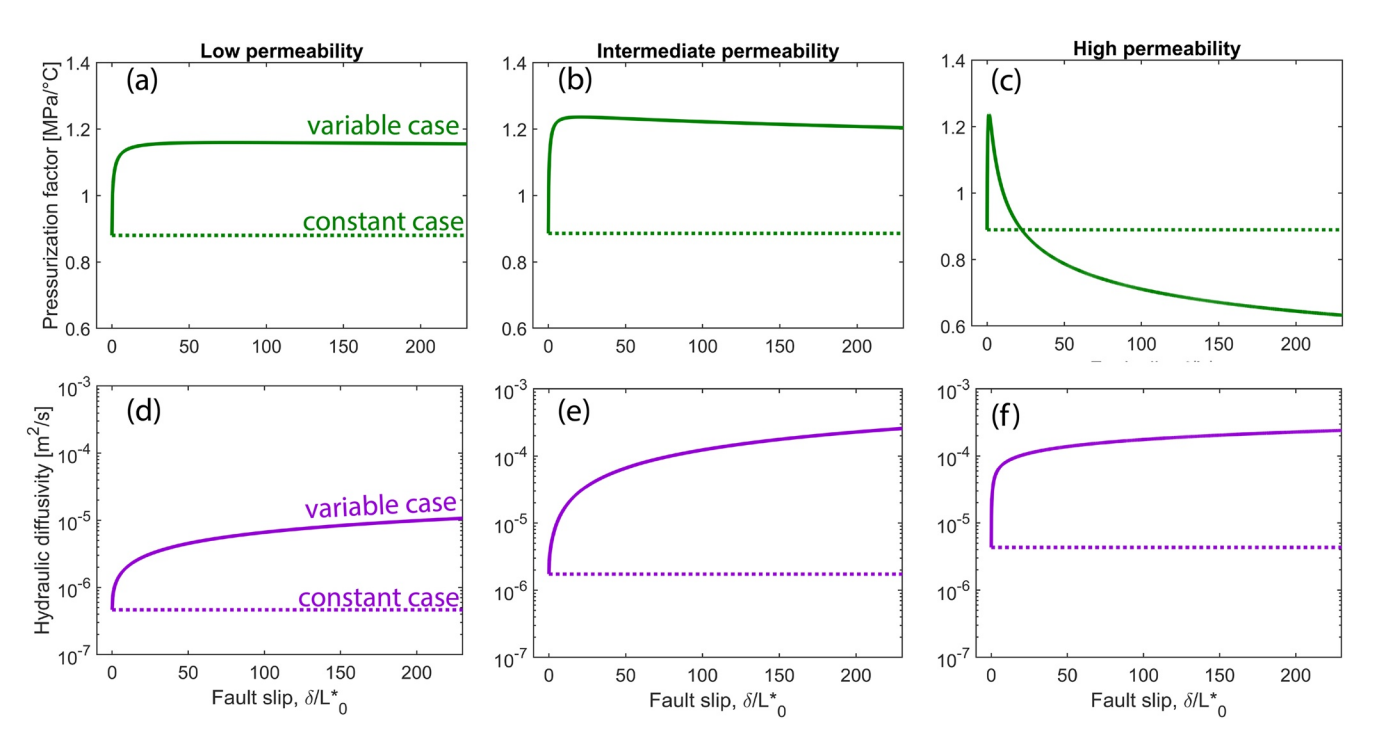


Figure 10. Pressurization factor (a–c) and hydraulic diffusivity (d–f) at the fault plane versus fault slip, for the low $(k_0 \sim 10^{-22} \text{ m}^2)$, intermediate $(k_0 \sim 10^{-21} \text{ m}^2)$ and high $(k_0 \sim 10^{-20} \text{ m}^2)$ permeability diabase. Solid lines and dotted lines represent variable and constant cases, respectively.

of heat diffusion overcoming the low heat production rate when shear stress drops by 94% from its initial value. The intermediate and high permeability diabase simulations show that ΔT evolves differently between the variable and constant cases. ΔT is greater in the variable case by $\delta/L_0^* \geq 110$ for the intermediate permeability and by $\delta/L_0^* \geq 0.5$ for the high permeability. The temperature evolution is directly related to the shear stress drops (through Equation 2) and demonstrating that even small changes in shear stress can result in significant changes in calculated fault zone temperature evolution. This effect is especially apparent at conditions where the variable and constant case models diverge early on, as in the case for the high permeability diabase. Heat transport does not differ significantly between these simulations as all heat transfer in the fault is conductive. Therefore, we can tie the temperature rise directly to the mechanical heat production on the fault plane. The permeability of the fault rocks can affect the heat transport when fluid advection is present, but since this model assumes that fluid advection is negligible over the duration of slip (Equation 2) it is not considered in this study.

The pressurization factor Λ and the hydraulic diffusivity ω are parameters that encapsulate the two elementary competing processes during TP, fluid pressurization and diffusion. Figure 10 compares how they evolve with fault slip at the fault plane for the varying permeability diabase. Λ increases rapidly at the early stages of fault slip $(\delta/L_0^* < 1)$ as temperature increases in the fault zone by shear heating (Figures 10a–10c). All three starting permeabilities show that with progressing fault slip Λ decreases, though at different rates that scale with the starting permeability of fault zone. The low permeability diabase exhibits a peak $\Lambda = 1.16$ MPa/°C (compare to the initial value of 0.89 MPa/°C). Λ decreases slightly with slip to a final value of 1.14 MPa/°C. This decrease is associated to the decrease in temperature in the fault zone (Figure 9d) as the temperature never exceeds 150°C, below the critical 200° C value where Λ decreases due to an increase in the compressibility of the fluid (Figures 5 and 6). The intermediate and high permeability diabase simulations do demonstrate a decrease in Λ that is associated with crossing the 200°C limit (Figure 5). A reaches a maximum, in both simulations, at 1.24 MPa/°C, though by the end of the simulation Λ equals to 1.2 and 0.63 MPa/°C for the intermediate and high permeability diabase, respectively. The high permeability diabase fault zone exhibits a smaller stress drop than the intermediate diabase fault zone (Figures 9b and 9c), which results in a higher temperature rise, and subsequently a greater reduction in Λ. The hydraulic diffusivity increases continuously for all three permeabilities (Figures 10d-10f), increasing by a factor (from its initial value ω_0) of ~23, ~147, and ~56 for the low, intermediate and high permeability diabase, by $\delta/L_0^* = 230$. The calculated increase in ω for each of the three simulations is attributed, mainly, to the increase in permeability

BADT ET AL. 14 of 22

nlinelibrary.wiley.com/doi/10.1029/2023JB026558 by Brown University Library, Wiley Online Library on [31/08/2023]. See the Terms

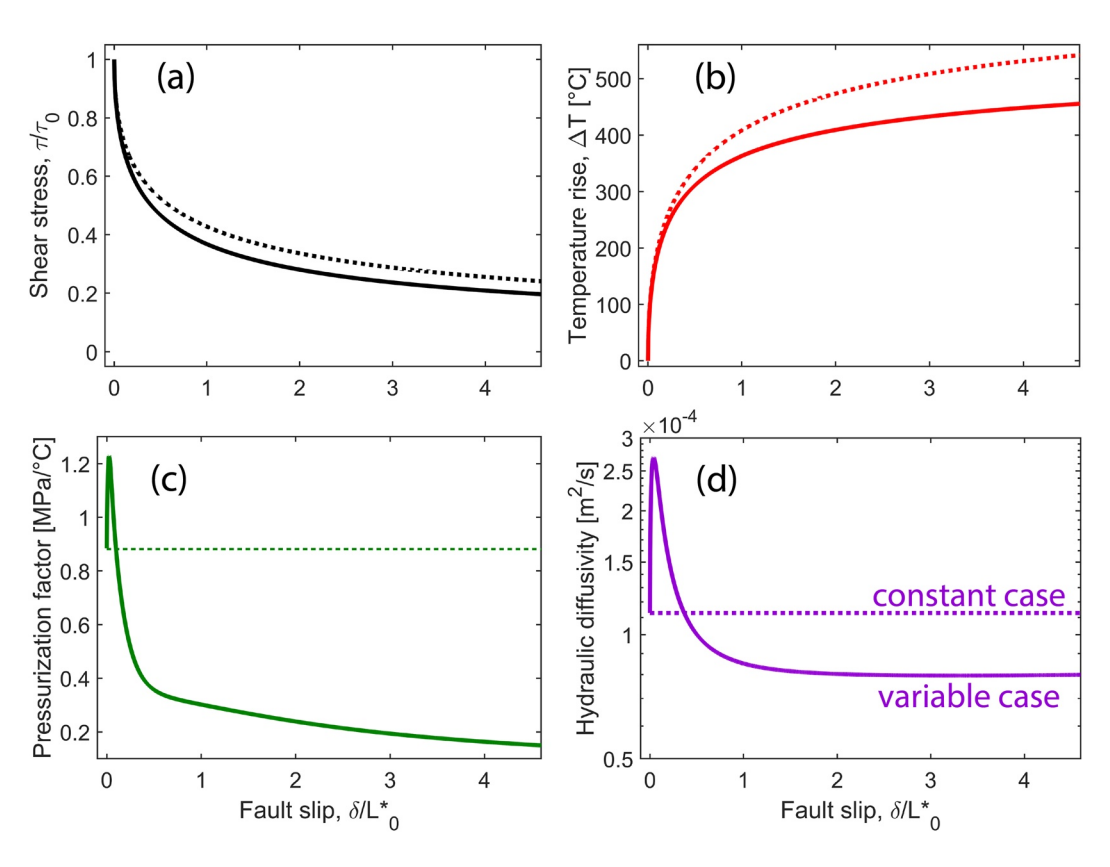


Figure 11. Variations of shear stress (a), temperature rise (b), pressurization factor (c) and hydraulic diffusivity (d) with fault slip for Westerly granite, at the fault plane, for the variable (solid curves) and constant (dotted curves) cases.

with pore pressure. For instance, permeability in the intermediate diabase increases by a factor of ~180 from its initial value, compared to factor increase of 64 and 110 for the low and high permeability diabase, respectively. An increase in storage capacity (mainly due to an increase in porosity and fluid compressibility) coupled with the decrease of dynamic fluid viscosity also control the evolution of hydraulic diffusivity, but to a lesser extent.

3.4. Westerly Granite

Westerly granite is now considered as the fault zone material for both the constant and variable cases of TP. Westerly granite was chosen due to the abundance of granite in the Earth's crust, making it a standard testing material in rock friction studies (e.g., Aubry et al., 2018; Barbery et al., 2021; Beeler et al., 1996; Blanpied et al., 1987; Byerlee, 1967; Dieterich, 1978; Goldsby & Tullis, 2011; Kilgore et al., 1993; Stesky et al., 1974; Tullis & Weeks, 1986). Permeability- and porosity-effective stress relations (Figure 4) were taken from Nasseri et al. (2009), for thermally-cracked Westerly granite at 650°C. Pore space in the rock is predominantly comprised of cracks (Nasseri et al., 2009). The granite fault zone simulations (variable and constant cases) initiate with a permeability $k_0 = 1.6 \times 10^{-19}$ m² and porosity $\phi_0 = 0.56\%$, a fault zone material with a higher permeability but comparable porosity to that included in the diabase simulations. Table 1 summarizes the mechanical, hydraulic and thermal properties for the Westerly granite simulations.

Figure 11 illustrates the evolution of shear stress, temperature, pressurization factor and hydraulic diffusivity with fault slip, calculated at the fault plane. For the Westerly granite, simulation results for the variable case show a greater stress drop (Figure 11a) and smaller temperature rise (Figure 11b) than the constant case. By the end of the simulation ($\delta/L_0^* \sim 4.6$), the shear stress drops by 80% (from its initial value) in the variable case, compared to 76% in the constant case. The temperature rise, by the end of the simulation, is thus more limited in the variable case, reaching $\Delta T = 456$ °C compared to $\Delta T = 542$ °C in the constant case. Figure 11c shows that the pressurization factor increases rapidly at the early stages of fault slip ($\delta/L_0^* < 0.023$), after which it decreases with slip as the fault zone temperature exceeds 200°C ($\Delta T > 125$ °C). The early transient increase in Δ results in a greater stress drop in the variable case, but later on a significant decrease in Δ with slip prevents further

BADT ET AL. 15 of 22

21699356, 2023, 8, Downlo

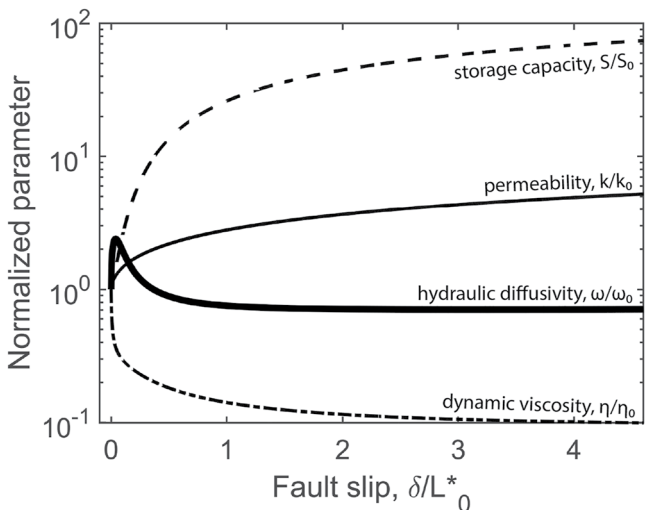


Figure 12. Hydraulic diffusivity (heavy solid line) and its components: permeability (thin solid line), storage capacity (dashed line) and dynamic fluid viscosity (dot-dashed line), versus fault slip. All parameters are normalized by their initial value (subscript zero). Hydraulic diffusivity $\omega = k/S\eta$.

frictional weakening, leading to an overall smaller stress drop in the granite, in comparison to the high permeability diabase (Figure 9c). Hydraulic diffusivity (ω) shows a different evolution with fault slip (Figure 11d) for the granite than the previous diabase simulations. As in the diabase simulations, ω increases rapidly at the early stages of slip, however, ω then decreases below its initial value ($\omega_0 \sim 10^{-4} \text{ m}^2/\text{s}$), equaling $\omega = 8 \times 10^{-5} \text{ m}^2/\text{s}$ by the end of the simulation. The reason for the decrease in ω is explained by looking at the evolution with slip of its components; permeability, storage capacity and dynamic fluid viscosity (Figure 12). Figure 12 examines the evolution of the hydraulic parameters at the fault plane, namely permeability, storage capacity and dynamic fluid viscosity, with fault slip. The increase in permeability and the decrease in viscosity, which contribute to an increase in ω , are counterbalanced by the significant increase of the storage capacity (S). Permeability increases and fluid viscosity decreases in the fault zone as pore pressure and temperature increase, respectively. The increase in storage capacity $S = \phi(\beta_f + \beta_\phi)$ is predominantly controlled by the increase in fluid compressibility β_f as the temperature in the fault zone increases above 200°C (Figure 6a). In general, the changes in the pressurization factor that occur early in the slip history, coupled with the relatively small changes in hydraulic diffusivity (compared to the high permeability diabase), result in an increasing difference between the constant case and the variable case with fault slip. Importantly, L_0^* for the granite (~ 0.01 m) is much larger than that

for the diabase ($\sim 10^{-4}$ m for the high permeability diabase). Therefore, the results for diabase (with $\delta/L_0^* > 200$) illustrate the difference between the constant and variable cases at larger displacements than the results for granite (with $\delta/L_0^* \leq 4.6$). The difference between the two cases is expected to be far greater in the granite when considering larger fault slip distances (due to the higher permeability of the granite), as both rock types represent a low porosity, crack-based hydraulic medium. However, due to the computational limitations in our model and the validity of the equations of state for water for the given temperature rise, we could not extend the simulation for granite to these larger slip distances.

3.5. Hanaore Fault Gouge

The variable case is explored here for fault zone material (Figure 13). The inputs for the model are based on fault core material from the active Hanaore fault in southwest Japan (Noda & Shimamoto, 2005). This fault zone is made of clay-rich foliated fault gouge, for which experimental data for the variations of permeability and porosity with effective pressure are available (Noda & Shimamoto, 2005). The permeability- and porosity-effective stress relations that were determined by Noda and Shimamoto (2005) include the full pressure cycling sequence. The data used to estimate the influence of effective stress on both permeability and porosity are taken from the post pressure cycling data, where the permeability and the porosity each follow a single permeability-effective stress and porosity-effective stress path. Pressure cycling is a common practice in experimental permeability and porosity tests, where permeability usually decreases by \sim 2–3 orders of magnitude from before to after the first pressure cycle (e.g., Wibberley & Shimamoto, 2003). During pressure cycling, the permeability and porosity are measured during both portions of the experiment where effective stress is increasing and decreasing: the difference in results is attributed to a specific stress history of the sample (Morrow et al., 1986). For the Hanaore gouge, the decrease in porosity after the first pressure cycle is less than an order of magnitude (Noda & Shimamoto, 2005). The gouge is more porous and permeable than the diabase and the granite considered before. The gouge's initial permeability and porosity (after pressure cycling) are $k_0 = 2.7 \times 10^{-19}$ m² and $\phi_0 = 17\%$, respectively, compared to those of the highest permeability diabase with $k_0 = 3.6 \times 10^{-20}$ m² and $\phi_0 = 1.17\%$, respectively (Figure 4).

Figure 13 illustrates the variations of shear stress, temperature rise, pressurization factor and hydraulic diffusivity, with fault slip, at the fault plane. The variable case predicts a slightly smaller stress drop $(\Delta \tau/\tau_0)$ than the constant case, whereby the end of the simulation $\Delta \tau/\tau_0 = 85\%$ in the variable case, compared to $\Delta \tau/\tau_0 = 88\%$ in the constant case (Figure 13a). This difference correlates with a greater temperature rise in the variable case ($\Delta T = 219^{\circ}$ C) compared to the constant case ($\Delta T = 181^{\circ}$ C), for $\delta/L_0^* = 21$ (Figure 13b). The pressurization factor in the variable case increases rapidly from an initial value of 1.14–1.5 MPa/°C over $\delta/L_0^* \leq 0.52$, after

BADT ET AL. 16 of 22

elibrary.wiley.com/doi/10.1029/2023JB026588 by Brown University Library, Wiley Online Library on [31/08/2023]. See the

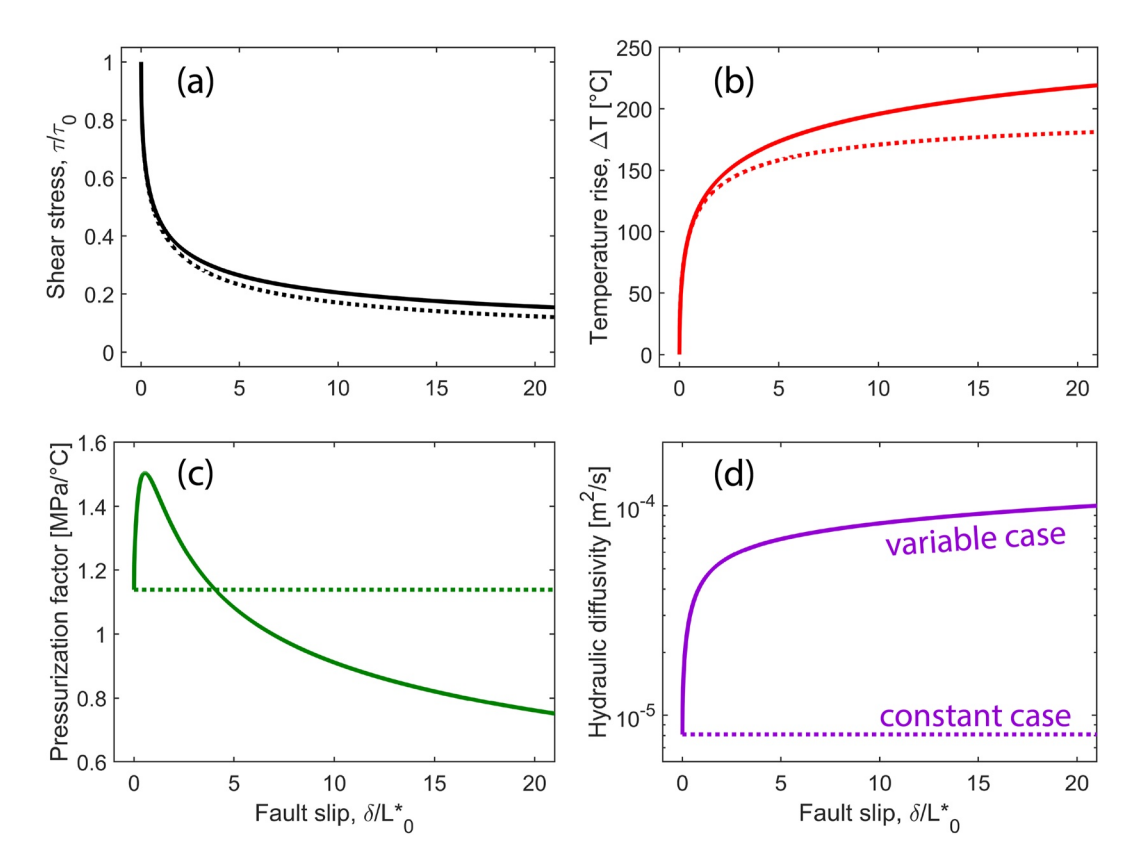


Figure 13. Variations of shear stress (a), temperature rise (b), pressurization factor (c) and hydraulic diffusivity (d) with fault slip, at the fault plane, for Hanaore fault gouge. The solid curves depict results for the variable case and the dotted curves for the constant case.

which it decreases gradually to 0.75 MPa/°C by the end of the simulation (Figure 13c). Note that the initial pressurization factor is greater for the gouge ($\Lambda_0 = 1.14$ MPa/°C) in comparison to the less porous diabase and granite (both have $\Lambda_0 = 0.89$ MPa/°C). The difference arises from the amount and type of pore space of the fault material. The porosity of the gouge ($\geq 17\%$) is greater than for the granite and diabase (<2%) and is considered as intergranular pores, in contrast to the fracture-type pore space in the diabase and granite. The pore space compressibility

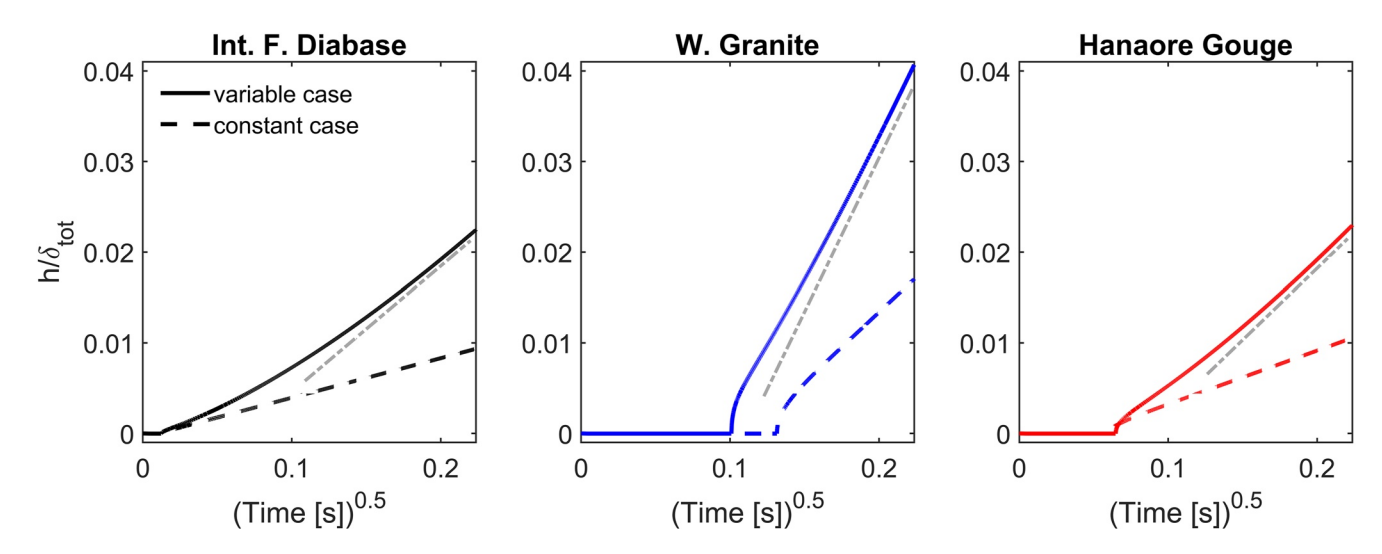


Figure 14. Calculated pressurized zone width h (normalized by the total fault slip $\delta_{tot} = 50$ mm) with the square root of time for the constant case and the variable case for intermediate permeability Frederick diabase (left), Westerly Granite (center) and Hanaore fault gouge (right). The gray dash-dotted lines depict a linear trend, showing that the variable case curves (solid lines) are nonlinear when plotted against the square root of time.

BADT ET AL. 17 of 22

 β_{ϕ} (Table 1) is an important parameter in the model, where both X and the storage capacity 3 (and thus hydraunic diffusivity) depend explicitly on β_{ϕ} . The porosity ϕ and the topology and connectivity of the pores both effect β_{ϕ} . Porosity topology is encapsulated in the constant b in the drained compressibility of the medium (Table 1):

$$\beta_d = \beta_s(1 + b\phi),\tag{16}$$

where β_s is the compressibility of the solid grains. We assign b = 10 for fracture porosity and b = 3 for intergranular pores (Renner et al., 2000). The pore space compressibility for an elastically-deforming fault zone is:

$$\beta_{\phi} = \frac{(\beta_d - \beta_s)(\beta_d + r\beta_s)}{\phi(1+r)\beta_d} - \beta_s. \tag{17}$$

Assuming r = 1 (Brantut & Mitchell, 2018; Rice, 2006), Equation 17 is reduced to:

$$\beta_{\phi} = \frac{\beta_d^2 - \beta_s^2}{2\phi\beta_d} - \beta_s \,. \tag{18}$$

Substituting Equation 16 in Equation 18 yields (after rearranging):

$$\beta_{\phi} = \beta_{s} \left[\frac{(1 + b\phi)^{2} - 1}{2\phi(1 + b\phi)} - 1 \right]. \tag{19}$$

We can compare the pore space compressibility of the crack-based granite and diabase to the more porous Hanaore fault gouge by plugging in the solid compressibility β_s , the initial porosity and the porosity topology constant b into Equation 19. For the crack-based porosity of Westerly granite and FD $\beta_{\phi} \sim 10^{-10}\,\mathrm{Pa^{-1}}$, while for the intergranular-porosity of the fault gouge $\beta_{\phi} \sim 10^{-11}\,\mathrm{Pa^{-1}}$. Thus, the pores of the more porous gouge are less compressible than the cracks in the diabase and granite, which in turn translates to a greater pressurization factor in the gouge. Furthermore, the less compressible pore space of the gouge maintains higher values of Λ (than for the crack-based hydraulic medium of the granite) even as the temperature in the fault zone exceeds 200°C when fault slip distances are $\delta/L_0^* > 1$.

3.6. Pressurized Zone Width

The width of the pressurized zone h is a measure of the distance over which high excess pore pressure, or over-pressurized pore fluid (above the background pore pressure p_0) builds up around the fault plane. We define it to be the maximum distance from the fault plane where pore pressure is at least 75% of the normal stress (Equation 13). Figure 14 depicts the calculated pressurized zone width versus the square root of time for the three rock types studied here; intermediate permeability diabase (Figure 14 left), Westerly granite (Figure 14 center) and Hanaore fault gouge (Figure 14 right). The width increases gradually with time for both the constant case and the variable case. h is consistently greater for the variable case than for the constant case and displays non-linear behavior in these plots. Greater h in the variable case simulations is the result of the increase in hydraulic diffusivity in the fault zone during TP, which allows excess pore pressure to build further away from the fault plane, while in the constant case hydraulic diffusivity remains in its initial state. This analysis shows that $h \propto t^{y}$, where y = 0.5 for the constant case and $y \sim 0.7$ for the variable case (Supporting Information S1). The higher power y in the variable case reflects the increase in hydraulic diffusivity during TP. The apparent linear trend for the variable case granite simulation (Figure 14 center) for $\sqrt{t} > 0.17$ reflects the near constant hydraulic diffusivity calculated in the latter stages of this simulation (Figure 11d). Because fluid pressurization is slower in the granite and gouge simulations, the calculated width remains zero in the early stages of slip. This is an artifact due to how h is defined, pore pressure builds up around the fault plane with the initiation of slip but does not reach 75% of the normal stress until some amount of slip.

4. Discussion

4.1. The Constant Versus Variable TP Model

Our analysis shows that shear stress evolution during TP is similar between the constant case and the variable case. However, the constant case captures the temperature rise, as calculated in the variable case, relatively well in specific simulations. The agreement between the two models represents a special case and not the general case. The variable case predicts that both the pressurization factor and hydraulic diffusivity, which encapsulate two competing processes, undergo significant increases from their initial values in the low permeability and low porosity diabase. The results from the variable case are similar to those in the constant case for the low permeability and low porosity diabase because the effects of the increases in both the pressurization factor and hydraulic diffusivity offset one another. In contrast, for the more porous and permeable fault gouge (Figure 13), and for the more permeable,

BADT ET AL. 18 of 22

onlinelibrary.wiley.com/doi/10.1029/2023JB026558 by Brown University Library, Wiley Online Library on [31/08/2023].

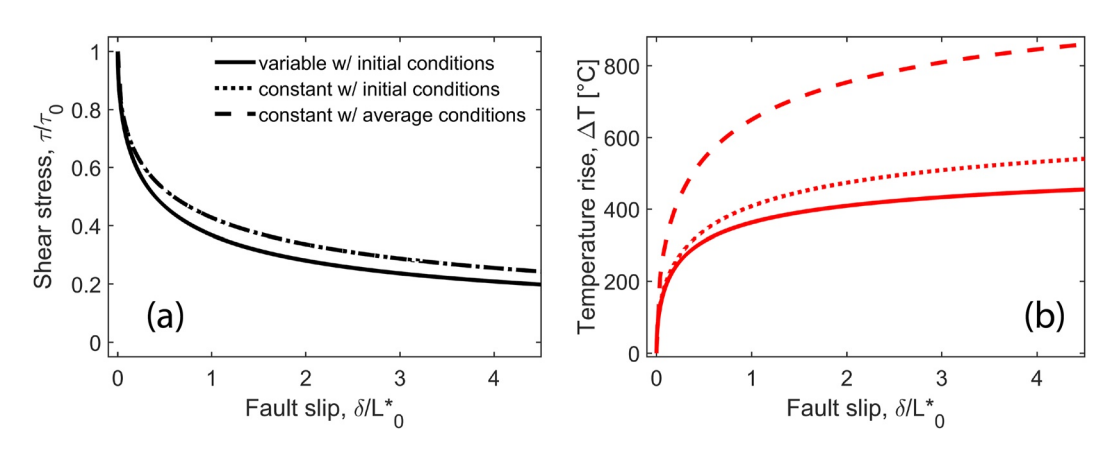


Figure 15. Shear stress (a) and temperature rise (b) with fault slip for the variable case (solid curves) and constant cases (dotted curves) with the same initial conditions ($T_0 = 25^{\circ}$ C and $p_0 = 25$ MPa) and for the constant case with average conditions from the range of temperature and pore pressure in the variable case ($T = 300^{\circ}$ C and p = 44 MPa). With average conditions the constant case grossly overestimates the temperature rise. The shear stress drop is slightly underestimated for both initial and average conditions.

low porosity (crack-based hydraulic medium) granite and high permeability diabase, the two models are significantly different. This is because the pressurization factor starts to decrease (when the temperatures in the fault zone exceed 200°C) while the hydraulic diffusivity increases continuously (in the gouge and diabase) or remains approximately constant (in the granite). Consequently, the increase in the pressurization factor is not counter-balanced by the increase in hydraulic diffusivity, as in the low and intermediate permeability diabase simulations (Figure 10). Thus, we suggest that the constant case model may be used successfully for modeling TP in very low permeability $(<10^{-20} \text{ m}^2)$ low porosity (<1%) fault zones. For fault rocks with higher porosity (>1%) or crack-dominated rocks with high permeability ($>10^{-20}$ m²) and low porosity (<1%) the variable case model needs to be considered in order to account for the multiple hydraulic and poroelastic feedbacks. The differences between the constant and variable cases appear early on during fault slip, at slip distances of $\delta/L_0^* < 1$, and become increasingly larger with fault slip. It is important to note that the constant and variable case models agree when starting from the same initial conditions, which are consistent with the starting temperature and pore pressure. In contrast, if parameters for the constant case are chosen to provide an estimate of average values along the pore pressure- and temperature-time evolution paths (e.g., Rice, 2006), then the differences between the two models may become significant. In this case, the constant case no longer provides a reasonable estimate of the temperature evolution. The constant case model parameters that may represent temporal-average conditions are the pressurization factor (Λ) and the hydraulic (ω) and thermal (κ) diffusivities (Equations 7–10). Figure 15 shows the shear stress and temperature evolution with fault slip for Westerly granite. Three simulations results are plotted: (a) the variable case with values of Λ , ω , and κ that correspond to a starting temperature of 75°C and pore pressure of 25 MPa; (b) the constant case with the same initial values of Λ , ω , and κ as (a); and (c) the constant case with Λ , ω , and κ that correspond to a temperature of 300°C and pore pressure of 44 MPa (Table 1), these are time-averaged values taken from the range of temperatures and pore pressures calculated in the variable case. Incorporating the "time-averaged" parameters is designed to compensate for the lack of evolution of these parameters in the constant case during TP (Brantut & Mitchell, 2018; Rice, 2006). The fault slip is normalized by the same length L_0^* , while for the time-averaged constant case it is normalized by the average length scale L_{ave}^* (where all parameters, per Equation 9, are time-averaged values). Here, the constant case with average conditions leads to much greater temperature rise than is predicted by the variable case or the constant case with the same initial ambient conditions (Figure 15). If one chooses to estimate shear stress and temperature at the fault plane with the constant case (or with Rice's (2006) analytical model), our results indicate that the model inputs should be chosen based on the initial temperature and pore pressure.

4.2. Pressurization Zone Width

The width of the pressurized zone around the fault plane h (or the over-pressured zone width) is greater in the variable case than in the constant case. The variable case predicts a wider pressurized zone that grows beyond that of the constant case (Figure 14), because the increase in hydraulic diffusivity during TP lead to $h \propto t^y$ where y = 0.5 in the constant case but $y \sim 0.7$ in the variable case. The faster growth of the pressurized zone around the fault plane for

BADT ET AL. 19 of 22

variable fault properties may have significant implications when considering a realistic fault zone structure where a damage zone with higher permeability (e.g., Faulkner et al., 2010; Rice, 2006; Stathas & Stefanou, 2023) bounds a localized fault core. Once the over-pressure zone reaches the hydraulic boundary between fault core and damage zone, the fault may transition from undrained conditions to drained condition (Mase & Smith, 1987; Stathas & Stefanou, 2023) faster than predicted by the constant case, when assuming a fault slipping at a constant rate. Stathas and Stefanou (2023) showed that, when considering a thin deforming gouge layer, once the over-pressured zoned reaches a hydraulic diffusive boundary, the fault can regain its frictional strength, even during coseismic slip rates, and cause the localization to migrate spatially. Thus, a pressure- and temperature-dependent hydraulic diffusivity can significantly change the frictional evolution of a TP-activated fault after the initial weakening stage.

4.3. Porosity Topology

The structure of fault rock porosity plays a significant role in the variable case TP model because it affects the pore space compressibility β_{ϕ} , which is an important parameter in both the pressurization factor and in the hydraulic diffusivity (Brantut & Mitchell, 2018). We adopt the parameterization of the porosity topology by Renner et al. (2000) in the factor b (Equations 16–19). Crack-dominated hydraulic structure which has a low porosity (<1%) but can have high permeability ($\geq 10^{-20}$ m²) has a higher pore space compressibility than a more porous gouge. This difference can lead to significant pressurization factor evolutions at higher temperatures (>200°C), which in turn affect the temperature rise estimates in the fault zone.

5. Conclusions

TP in fault zones includes various feedbacks owing to the dependency of poroelastic and hydraulic parameters on pore pressure and temperature. The analytical solution by Rice (2006), which assumes constant hydraulic and thermal properties (the *constant case*) cannot account for the significant poromechanical response of the fault zone during TP and the subsequent evolution of temperature, fluid properties and the pressurization factor. The general numerical solution presented in our study uses properties that are temperature- and pressure-dependent (the *variable case*).

Nonetheless, the *constant case* model captures the shear stress evolution for a localized fault with slip reasonably well. For example, calculated stress drops in the *variable case* models are comparable to those calculated with the *constant case* model *if* values of pressurization factor, hydraulic and thermal diffusivities are chosen to correspond to the starting conditions of the fault zone in the constant case. In contrast, choosing these values based on an average of each parameter's expected range over the course of TP duration may lead to significant errors, particularly in the temperature rise estimates during TP. Understanding the temperature rise during earthquakes is of great importance when interpreting the thermal evolution of natural fault zones. For instance, when thermal history of relict slip surfaces is estimated with various proxies, like organic biomarker maturation (e.g., Savage et al., 2014) and thermochronology (e.g., Ault et al., 2019).

The *variable case* model represents a more general model for TP, as it captures the full hydraulic-poroelastic response of the fault zone rocks and fluids. The constant case represents a special case for low porosity (<1%) and low permeability ($<10^{-20}$ m²) fault rocks. In low porosity, low permeability rocks, results of simulations with the *constant case* are similar to those of the variable case model because the effects of evolution in the parameters that control fluid pressurization and hydraulic diffusivity happen to offset one another. However, this balanced offset does not occur in *variable case* models for more porous and permeable rocks or more permeable ($>10^{-20}$ m²) crack-dominated fault rocks (with porosity <1%). The fault zone temperature in these rock types can easily exceed 200°C, in which case the pressurization factor decreases and this change is not offset by changes in other parameters, namely hydraulic diffusivity which can either remain nearly constant (as in the cracked granite simulations) or increase continuously with temperature and pore pressure. Consequently, for more porous or permeable fault rocks, the *variable case* provides a more accurate time-evolution of pore pressure and temperature in the fault zone during TP. The type of fault rock porosity, crack-dominated or intergranular pore-dominated (parameterized by the factor *b* in Equation 19), has a significant effect on both the pressurization factor and the hydraulic diffusivity, and should be considered when simulating TP, either numerically or experimentally.

The width of the zone of over-pressurized fluid h scales with time as $h \propto t^{0.7}$. This increase from the typical diffusional timescale scaling of $t^{0.5}$ is due to the increase in hydraulic diffusivity with pore pressure and temperature during frictional sliding with TP. The variable case predicts that a localized fault will transition from undrained to

BADT ET AL. 20 of 22



Journal of Geophysical Research: Solid Earth

10.1029/2023JB026558

drained conditions sooner than expected from the constant case, when considering a hydraulically heterogeneous fault zone, where a low permeability fault core is bounded by a more permeable damage zone. Subsequently, the variable case TP would predict shorter-lived TP events than predicted by the constant case. This effect is especially important when considering TP at low temperatures ($<200^{\circ}$ C).

Data Availability Statement

Matlab codes for this study are available as a public record at Badt (2023).

Acknowledgments References

We would like to thank the anonymous associate editor, Antoine B. Jacquey and another anonymous reviewer for their comments which improved this paper considerably. We would also like to thank E. Marc Parmentier for the early discussions that helped lay the foundations for this study. This study was supported by the Southern California Earthquake Center under Grant 18156. Matlab codes for this study are available as a public

records at https://doi.org/10.26300/

zqvn-fh24.

- Acosta, M., Passelègue, F. X., Schubnel, A., & Violay, M. (2018). Dynamic weakening during earthquakes controlled by fluid thermodynamics.

 Nature Communications. 9(1), 3074. https://doi.org/10.1038/s41467-018-05603-9
- Andrews, D. J. (2002). A fault constitutive relation accounting for thermal pressurization of pore fluid. *Journal of Geophysical Research*, 107(B12), ESE-15–ESE-18. https://doi.org/10.1029/2002jb001942
- Aubry, J., Passelègue, F. X., Deldicque, D., Girault, F., Marty, S., Lahfid, A., et al. (2018). Frictional heating processes and energy budget during laboratory earthquakes. *Geophysical Research Letters*, 45(22), 12–274. https://doi.org/10.1029/2018gl079263
- Ault, A. K., Gautheron, C., & King, G. E. (2019). Innovations in (U-Th)/He, fission track, and trapped charge thermochronometry with applications to earthquakes, weathering, surface-mantle connections, and the growth and decay of mountains. *Tectonics*, 38(11), 3705–3739. https://doi.org/10.1029/2018tc005312
- Aydin, A. (2000). Fractures, faults, and hydrocarbon entrapment, migration and flow. Marine and Petroleum Geology, 17(7), 797–814. https://doi.org/10.1016/s0264-8172(00)00020-9
- Badt, N. Z. (2023). Codes for numerical thermal pressurization [Software]. Brown University Open Data Collection. Brown Digital Repository. Brown University Library. https://doi.org/10.26300/zqvn-fh24
- Badt, N. Z., Tullis, T. E., Hirth, G., & Goldsby, D. L. (2020). Thermal pressurization weakening in laboratory experiments. *Journal of Geophysical Research: Solid Earth*, 125(5), e2019JB018872. https://doi.org/10.1029/2019jb018872
- Barbery, M. R., Chester, F. M., & Chester, J. S. (2021). Characterizing the distribution of temperature and normal stress on flash heated granite surfaces at seismic slip rates. *Journal of Geophysical Research: Solid Earth*, 126(5), e2020JB021353. https://doi.org/10.1029/2020jb021353
- Beeler, N. M., Tullis, T. E., Blanpied, M. L., & Weeks, J. D. (1996). Frictional behavior of large displacement experimental faults. *Journal of Geophysical Research*, 101(B4), 8697–8715. https://doi.org/10.1029/96jb00411
- Bernabé, Y., Mok, U., & Evans, B. (2003). Permeability-porosity relationships in rocks subjected to various evolution processes. *Pure and Applied Geophysics*, 160(5), 937–960. https://doi.org/10.1007/pl00012574
- Bizzarri, A., & Cocco, M. (2006). A thermal pressurization model for the spontaneous dynamic rupture propagation on a three-dimensional fault: 1. Methodological approach. *Journal of Geophysical Research*, 111(B5), B05303. https://doi.org/10.1029/2005jb003862
- Blanpied, M. L., Tullis, T. E., & Weeks, J. D. (1987). Frictional behavior of granite at low and high sliding velocities. *Geophysical Research Letters*, 14(5), 554–557. https://doi.org/10.1029/gl014i005p00554
- Brantut, N. (2021). Dilatancy toughening of shear cracks and implications for slow rupture propagation. *Journal of Geophysical Research: Solid Earth*, 126(11), e2021JB022239. https://doi.org/10.1029/2021jb022239
- Brantut, N., & Mitchell, T. M. (2018). Assessing the efficiency of thermal pressurization using natural pseudotachylyte-bearing rocks. *Geophysical Research Letters*, 45(18), 9533–9541. https://doi.org/10.1029/2018gl078649
- Byerlee, J. D. (1967). Frictional characteristics of granite under high confining pressure. *Journal of Geophysical Research*, 72(14), 3639–3648. https://doi.org/10.1029/jz072i014p03639
- Chester, F. M., & Chester, J. S. (1998). Ultracataclasite structure and friction processes of the Punchbowl fault, San Andreas system, California. *Tectonophysics*, 295(1–2), 199–221. https://doi.org/10.1016/s0040-1951(98)00121-8
- Chester, J. S., & Goldsby, D. L. (2003). Microscale characterization of natural and experimental slip surfaces relevant to earthquake mechanics (SCEC Annual Progress Report 2003). Southern California Earthquake Center (SCEC).
- Dieterich, J. H. (1978). Time-dependent friction and the mechanics of stick-slip. In *Rock friction and earthquake prediction* (pp. 790–806). Birkhäuser.
- Faulkner, D. R., Jackson, C. A. L., Lunn, R. J., Schlische, R. W., Shipton, Z. K., Wibberley, C. A. J., & Withjack, M. O. (2010). A review of recent developments concerning the structure, mechanics and fluid flow properties of fault zones. *Journal of Structural Geology*, 32(11), 1557–1575. https://doi.org/10.1016/j.jsg.2010.06.009
- Faulkner, D. R., Mitchell, T. M., Behnsen, J., Hirose, T., & Shimamoto, T. (2011). Stuck in the mud? Earthquake nucleation and propagation through accretionary forearcs. *Geophysical Research Letters*, 38(18). https://doi.org/10.1029/2011gl048552
- Fondriest, M., Mecklenburgh, J., Passelegue, F. X., Artioli, G., Nestola, F., Spagnuolo, E., & Di Toro, G. (2020). Pseudotachylyte alteration and the rapid fade of earthquake scars from the geological record. *Geophysical Research Letters*, 47(22), e2020GL090020. https://doi.org/10.1029/2020gl090020
- Fredrich, J. T., & Wong, T. F. (1986). Micromechanics of thermally induced cracking in three crustal rocks. *Journal of Geophysical Research*, 91(B12), 12743–12764. https://doi.org/10.1029/jb091ib12p12743
- Fujiwara, T., Kodaira, S., No, T., Kaiho, Y., Takahashi, N., & Kaneda, Y. (2011). The 2011 Tohoku-Oki earthquake: Displacement reaching the trench axis. Science, 334(6060), 1240. https://doi.org/10.1126/science.1211554
- Garagash, D. I. (2012). Seismic and aseismic slip pulses driven by thermal pressurization of pore fluid. *Journal of Geophysical Research*, 117(B4), B04314. https://doi.org/10.1029/2011jb008889
- Goldsby, D. L., & Tullis, T. E. (2011). Flash heating leads to low frictional strength of crustal rocks at earthquake slip rates. *Science*, 334(6053), 216–218. https://doi.org/10.1126/science.1207902
- Kanamori, H., Heaton, T. H., & Rundle, J. B. (2000). Microscopic and macroscopic physics of earthquakes. In Geophysical monograph (Vol. 120, pp. 147–164). American Geophysical Union.
- Kilgore, B. D., Blanpied, M. L., & Dieterich, J. H. (1993). Velocity dependent friction of granite over a wide range of conditions. *Geophysical Research Letters*, 20(10), 903–906. https://doi.org/10.1029/93g100368

BADT ET AL. 21 of 22

- Kirkpatrick, J. D., & Rowe, C. D. (2013). Disappearing ink: How pseudotachylytes are lost from the rock record. *Journal of Structural Geology*, 52, 183–198. https://doi.org/10.1016/j.jsg.2013.03.003
- Kirkpatrick, J. D., Shipton, Z. K., & Persano, C. (2009). Pseudotachylytes: Rarely generated, rarely preserved, or rarely reported? Bulletin of the Seismological Society of America, 99(1), 382–388. https://doi.org/10.1785/0120080114
- Lachenbruch, A. H. (1980). Frictional heating, fluid pressure, and the resistance to fault motion. *Journal of Geophysical Research*, 85(B11), 6097–6112. https://doi.org/10.1029/jb085jb11p06097
- Lee, T. C., & Delaney, P. T. (1987). Frictional heating and pore pressure rise due to a fault slip. *Geophysical Journal International*, 88(3), 569–591. https://doi.org/10.1111/j.1365-246x.1987.tb01647.x
- Mase, C. W., & Smith, L. (1984). Pore-fluid pressures and frictional heating on a fault surface. Pure and Applied Geophysics, 122(2–4), 583–607. https://doi.org/10.1007/bf00874618
- Mase, C. W., & Smith, L. (1987). Effects of frictional heating on the thermal, hydrologic, and mechanical response of a fault. *Journal of Geophysical Research*, 92(B7), 6249–6272. https://doi.org/10.1029/jb092ib07p06249
- Morrow, C. A., Zhang, B. C., & Byerlee, J. D. (1986). Effective pressure law for permeability of Westerly granite under cyclic loading. *Journal of Geophysical Research*, 91(B3), 3870–3876. https://doi.org/10.1029/jb091ib03p03870
- Nasseri, M. H. B., Schubnel, A., Benson, P. M., & Young, R. P. (2009). Common evolution of mechanical and transport properties in thermally cracked westerly granite at elevated hydrostatic pressure. Pure and Applied Geophysics, 166(5), 927–948. https://doi.org/10.1007/s00024-009-0485-2
- NIST Chemistry Webbook, SRD 69. (2022). Thermophysical properties of fluid systems. (n.d.). Retrieved from https://webbook.nist.gov/chemistry/fluid/#
- Noda, H., & Lapusta, N. (2010). Three-dimensional earthquake sequence simulations with evolving temperature and pore pressure due to shear heating: Effect of heterogeneous hydraulic diffusivity. *Journal of Geophysical Research*, 115(B12), B12314. https://doi.org/10.1029/2010jb007780
- Noda, H., & Shimamoto, T. (2005). Thermal pressurization and slip-weakening distance of a fault: An example of the Hanaore fault, southwest Japan. Bulletin of the Seismological Society of America, 95(4), 1224–1233. https://doi.org/10.1785/0120040089
- Passelègue, F. X., Goldsby, D. L., & Fabbri, O. (2014). The influence of ambient fault temperature on flash-heating phenomena. Geophysical Research Letters, 41(3), 828–835. https://doi.org/10.1002/2013g1058374
- Phillips, N. J., Rowe, C. D., & Ujiie, K. (2019). For how long are pseudotachylytes strong? Rapid alteration of basalt-hosted pseudotachylytes from a shallow subduction complex. Earth and Planetary Science Letters, 518, 108–115. https://doi.org/10.1016/j.epsl.2019.04.033
- Renner, J., Evans, B., & Hirth, G. (2000). On the rheologically critical melt fraction. Earth and Planetary Science Letters, 181(4), 585–594. https://doi.org/10.1016/s0012-821x(00)00222-3
- Rice, J. R. (2006). Heating and weakening of faults during earthquake slip. *Journal of Geophysical Research*, 111(B5), B05311. https://doi.org/10.1029/2005ib004006
- Robertson, E. C. (1988). Thermal properties of rocks (Open-file report 88-441). USGS.
- Savage, H. M., Polissar, P. J., Sheppard, R., Rowe, C. D., & Brodsky, E. E. (2014). Biomarkers heat up during earthquakes: New evidence of seismic slip in the rock record. *Geology*, 42(2), 99–102. https://doi.org/10.1130/g34901.1
- Scholz, C. H. (2002). The mechanics of earthquakes and faulting. Cambridge University Press.
- Sibson, R. H. (1973). Interactions between temperature and pore-fluid pressure during earthquake faulting and a mechanism for partial or total stress relief. *Nature: Physical Science*, 243(126), 66–68. https://doi.org/10.1038/physci243066a0
- Sibson, R. H. (1975). Generation of pseudotachylyte by ancient seismic faulting. Geophysical Journal International, 43(3), 775–794. https://doi.org/10.1111/j.1365-246x.1975.tb06195.x
- Sibson, R. H. (2003). Thickness of the seismic slip zone. Bulletin of the Seismological Society of America, 93(3), 1169–1178. https://doi.org/10.1785/0120020061
- Sibson, R. H., Toy, V. G., Abercrombie, R., & McGarr, A. (2006). The habitat of fault-generated pseudotachylyte: Presence vs. absence of friction-melt. In *Geophysical monograph* (Vol. 170). American Geophysical Union.153
- Stathas, A., & Stefanou, I. (2023). Fault friction under thermal pressurization during large seismic-slip: Numerical analyses and extension of the model of frictional slip. *International Journal of Mechanical Sciences*, 248, 108184. https://doi.org/10.1016/j.ijmecsci.2023.108184
- Stesky, R. M., Brace, W. F., Riley, D. K., & Robin, P. Y. (1974). Friction in faulted rock at high temperature and pressure. *Tectonophysics*, 23(1–2), 177–203. https://doi.org/10.1016/0040-1951(74)90119-x
- Tullis, T. E. (2015). Mechanisms for friction of rock at earthquake slip rates, Chapter 5. In H. Kanamori (Ed.), *Treatise on geophysics*, v.4, *Earthquake seismology* (pp. 131–152). Elsevier Ldt.
- Tullis, T. E., & Weeks, J. D. (1986). Constitutive behavior and stability of frictional sliding of granite. *Pure and Applied Geophysics*, 124(3), 383–414. https://doi.org/10.1007/bf00877209
- Viesca, R. C., & Garagash, D. I. (2015). Ubiquitous weakening of faults due to thermal pressurization. *Nature Geoscience*, 8(11), 875–879. https://doi.org/10.1038/ngeo2554
- Wang, H. F. (2017). Theory of linear poroelasticity with applications to geomechanics and hydrogeology. Princeton University Press.
- Wibberley, C. A., & Shimamoto, T. (2003). Internal structure and permeability of major strike-slip fault zones: The Median Tectonic Line in Mie Prefecture, Southwest Japan. *Journal of Structural Geology*, 25(1), 59–78. https://doi.org/10.1016/s0191-8141(02)00014-7
- Wibberley, C. A., & Shimamoto, T. (2005). Earthquake slip weakening and asperities explained by thermal pressurization. *Nature*, 436(7051), 689–692. https://doi.org/10.1038/nature03901
- Yao, L., Ma, S., & Di Toro, G. (2023). Coseismic fault sealing and fluid pressurization during earthquakes. *Nature Communications*, 14(1), 1136. https://doi.org/10.1038/s41467-023-36839-9

BADT ET AL. 22 of 22

The pressure- and temperature-dependence of thermal pressurization in localized faults

- 4 Nir Z. Badt, Christian Huber, Greg Hirth and Terry E. Tullis
- 5 Brown University, Providence RI, USA

6

7

3

| | $\overline{}$ | | | | | | |
|-----|---------------|---------------|--------------|---|--------|---|----|
| - 1 | Ι. | $\overline{}$ | \mathbf{r} | - | \sim | n | +- |
| | | 1 1 | | | _ | | |
| , | _ | U | | L | _ | | ts |

| 8 | 1 | Sup | plemental materialsplemental materials | 1 |
|----|---|-----|---|---|
| | | | Numerical errors for different slip rates | |
| 10 | 1 | .2 | Pressurized zone width scaling | 2 |

11 12

13

1 Supplemental materials

- 14 1.1 Numerical errors for different slip rates
- Figure 1 presents the calculated numerical error for temperature (Err_T) over simulated time for three
- different simulations of intermediate permeability Frederick diabase fault rock. Each simulation was
- performed with a grid spacing of $\Delta x = 10^{-6}$ m, a timestep size of $\Delta t = 10^{-7}$ s but with different slip
- rates: 1, 0.1 and 0.01 m/s. The maximum error occurs early in the simulations but their magnitude
- decreases with slip rate: $Err_T^{max} = 12.16 \%$ for v = 1 m/s; $Err_T^{max} = 1.85 \%$ for v = 0.1 m/s; and
- 20 $Err_T^{max} = 0.21 \%$ for v = 0.01 m/s.

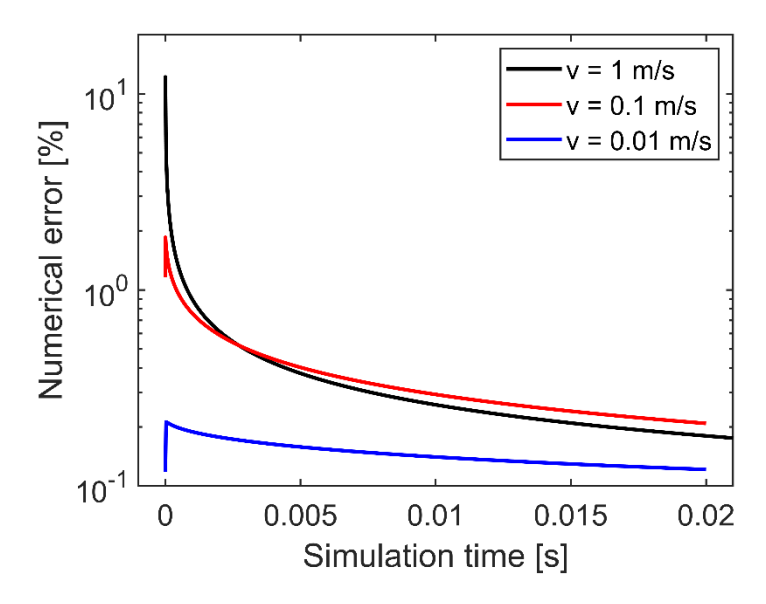


Figure 1. Numerical error for temperature (Err_T) over simulation time for different simulated slip rates, 1 m/s (black curve), 0.1 m/s (red curve) and 0.01 m/s (blue curve).

1.2 Pressurized zone width scaling

Figure 2 depicts the pressurized zone width h (normalized by the total slip distance $\delta_{tot}=50$ mm) versus the time raised to the power of 0.7 for the variable case simulations. After the initial non-linearity when each curve increases above $h/\delta_{tot}=0$, the curves for all simulated rock types display a linear trend for the scaling of $h{\sim}t^{0.7}$.

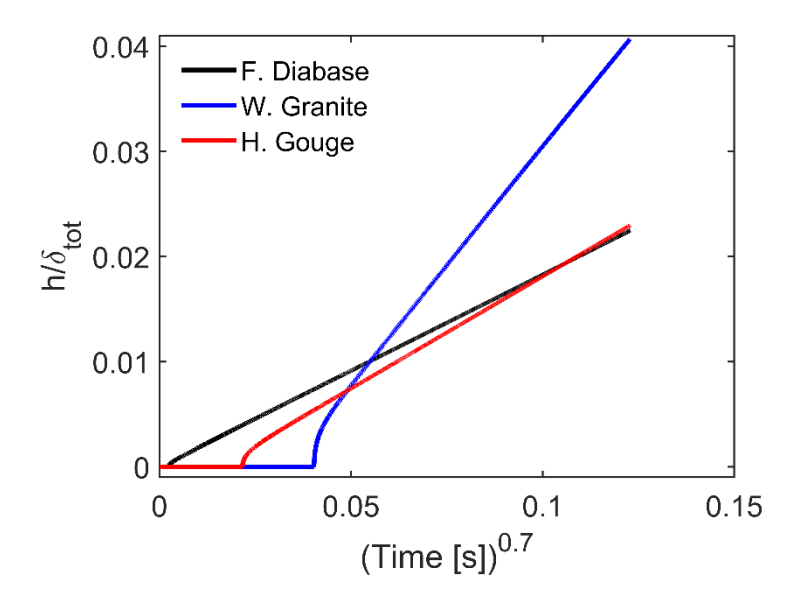


Figure 2. Pressurization zone width (h) versus time raised to the power 0.7 depicting linear trends over the majority of the simulated time.